공학박사 학위논문

Application of neural network potential to accurate prediction of thermal properties of materials

재료의 열물성에 대한 정확한 예측을 위한 인공신경망 퍼텐셜의 응용

2023년 2월

서울대학교 대학원
재료공학부
이 경 풍

공학박사 학위논문

Application of neural network potential to accurate prediction of thermal properties of materials

재료의 열물성에 대한 정확한 예측을 위한 인공신경망 퍼텐셜의 응용

2023년 2월

서울대학교 대학원
재료공학부
이 경 풍

Application of neural network potential to accurate prediction of thermal properties of materials

재료의 열물성에 대한 정확한 예측을 위한 인공신경망 퍼텐셜의 응용

지도교수 한 승 우

이 논문을 공학박사 학위논문으로 제출함

2023년 2월

서울대학교 대학원

재료공학부

이 경 풍

이경풍의 박사 학위논문을 인준함

2022년 12월

위 원 장	정 인 호	(인)
부위원장	한 승 우	(인)
위 원	장 혜 진	(인)
위 원	이 병 주	(인)
위 원	최 운 이	(인)

Abstract

With the development of the density-functional theory (DFT) and ever-increasing computational capacity, an accurate prediction of thermal properties of materials becomes computationally feasible. When DFT calculations are combined with the theoretical methodologies, such as Boltzmann transport equations, thermodynamic integration, and semigrand ensemble simulations, the lattice thermal conductivity and phase diagram can be calculated without experimental inputs. However, a huge amount of computational resources required for calculating these thermal properties hinders the exploration of a wide range of systems. In recent years, the machine-learned potentials (MLPs) are getting much attentions as a surrogate model of DFT, providing near-DFT accuracy at a fraction of computational cost. Whereas MLPs have been proven to predict thermal properties in *ab initio* accuracy, more investigations are required for calculation of the lattice thermal conductivity for a wide range of crystal symmetries, as well as construction of multi-component phase diagrams.

In this dissertation, calculation of thermal properties using neural network interatomic potentials (NNPs) is demonstrated. First, lattice thermal conductivity is calculated for crystal structures that have diverse symmetries and wide range of conductivity. To construct transferable data sets for training NNPs, three methods are tested: random displacement, superposition of phonon eigenmodes, and *ab initio* molecular dynamics. 25 materials are benchmarked on the best data set to evaluate the accuracy and computational cost compared with the pure-DFT approaches. The test reveals that while 2-10 fold computational savings are achieved, most of the computational resources are put into the construction of data set. By reducing the data set, at maximum 50-fold acceleration is obtained compared to the pure-DFT approach with marginal compromise in accuracy. Next, the full phase diagram of MgO–CaO eutectic system is constructed by calculating the free energy of rocksalt and liquid phases with molecular

dynamics simulations. They are trained on NVT- and NPT-MD simulations at selected stoichiometry to span the relevant temperature, composition, and phase domain. In addition, to see the effect of approximations on the DFT exchange-correlation energies, we generate data set using the two functional, PBE and SCAN, and compare them in the phase diagram. Notably, phase boundaries predicted by SCAN-NNP are close to the experiments, and total computational cost is reduced by more than 1,000-fold compared with fully DFT approach. Finally, phase transition of HfO_2 is studied at atmospheric pressure, utilizing only its chemical composition as the starting point, to test the strategy for constructing fully theoretical phase diagram. This can be accomplished by incorporating crystal structure prediction algorithms to identify candidate phases. Afterward, the temperature-dependent stability and phase transitions are revealed through MD simulations and free energy calculations performed with NNPs, which are on the candidate phases. By accelerating *ab initio* prediction of stable phases and their properties employing NNPs, we believe this work will be extended to a self-contained computational laboratory for materials exploration.

keywords: machine-learned potential, neural network interatomic potential, lattice thermal conductivity, free energy calculations, phase diagram

student number: 2016-20806

Contents

List of Tables

List of Figures

Chapter 1

Introduction

1.1 Overview

Thermal properties are at the heart of materials science and engineering. Lattice thermal conductivity dominates heat transfer in insulators and semiconductors, and the required value varies depending on the purpose; thermoelectric materials or heat sink ceramics require low or high thermal conductivity, respectively. In the meanwhile, the phase diagram allows one to predict states of matter that can change under input/output of heat. Despite the usefulness of these thermal properties, only a subset of the materials have been studied due to the vast experimental effort and cost, compared to the possible combinations of chemical elements and stoichiometry. In these motivations, attempts to explore the unknown materials space in order to discover new materials have continued [1–4].

Density-functional theory (DFT) calculations have been widely adopted to address phenomena in experiments or to predict material properties. This is because DFT provides sufficient accuracy without empirical parameters. Despite the successes and usefulness of DFT, the main bottleneck stems from the expensive computational cost that limits time and length scale of the simulations. Thus, realistic simulations such as crystallization of phase-change materials [5], thermal transport via interfaces [6], and free

energy calculations on alloys [7] are practically prohibited within DFT.

To overcome these limitations, force fields are often fitted toward DFT calculations to reproduce accurate energy and forces. Since their computational cost is much inexpensive compared to DFT, they can simulate the large-scale reactions such as dry oxidation of silicon [8]. While the force field methods are formulated with interaction terms that are physically sensible, their pre-determined functional form has often limited their transferability toward other systems or simulation domains. Efforts have been made to address these limitations by modifying the formalism, thereby broadening the scope of force field methods [9, 10].

Recently, machine-learned potentials (MLPs) have attracted much attention as surrogate models of DFT calculations as they provide *ab initio* accuracy with a fraction of computational cost [11, 12]. A main feature of MLP is that the model is mathematically flexible so that it is applicable to most of the systems ranging from metallic to covalent and ionic systems. A wide range of molecular simulations have been accelerated by MLPs: crystallization of phase change materials [5], reactions at the interface between Si and Ni [13], crystal structure prediction [14], and light emission spectra of core-shell quantum dot [15].

MLPs are also useful for thermal properties of materials. Although successful in calculating lattice thermal conductivity for a variety of materials, a standard approach for generating data set is lacking, and the computational savings when employing MLPs are not fully discussed. In addition, phase diagrams are mainly demonstrated on unary systems while studies on binary and multinary systems are still lacking. Therefore, it is timely to further demonstrate calculation of thermal properties using MLPs, including accurate and computationally efficient prediction of lattice thermal conductivity [16] and construction of multinary phase diagram [17].

Achieving these goals requires exploring and understanding the effect of the data set on the final MLP. First of all, the data set should span the target simulation domain and at the same time best represent it. Conventional approaches exploit human

intuition for constructing and augmenting the data set, while recent approaches use machine-learning techniques such as uncertainty estimations to append the data that are relevant to the target simulations. Furthermore, MLPs have been mostly trained on DFT calculations with approximations of exchange-correlation energy by Perdew-Burke-Ernzerhof (PBE) [18]. As this functional often becomes erroneous in predicting thermal properties, more accurate and advanced functional such as SCAN [19] or even the level of theory beyond DFT has been employed to improve accuracy of the final model.

1.2 Goal of the dissertation

This dissertation aims to calculate thermal properties of materials using neural network interatomic potentials (NNPs), including lattice thermal conductivity (κ_l) and composition-temperature phase diagram. In detail, κ_l at 300 K is calculated for crystals with diverse symmetries and elemental combinations by solving Boltzmann transport equation under relaxation-time approximation, followed by validations on lattice dynamics and phonon lifetime. Then the phase diagram of MgO–CaO pseudo-binary system is calculated for a wide range of composition and temperature, employing thermodynamic integration and semigrand ensemble methods based on MD simulations; validations on, for example, melting point of the pure MgO and CaO phases are preceded and compared to the available literature. By demonstrating accurate prediction of κ_l and construction of the phase diagram, this dissertation would further extend the application range of MLPs toward thermal properties of materials.

1.3 Organization of the dissertation

This dissertation is organized in 6 chapters. Chapter 1 is the introduction which gives an overview on machine-learned potentials, thermal properties of materials, and the goal of this dissertation. In Chapter 2, theoretical backgrounds for density-functional theory and machine-learned potential are briefly discussed. Chapter 3 shows the application of NNPs for lattice thermal conductivities. Then Chapter 4 demonstrates construction of a full phase diagram including melting point for MgO–CaO pseudo-binary system. In Chapter 5, approaches toward phase diagrams when there is no phase information are tested for phase transition of HfO_2. Finally, Chapter 6 summarizes this dissertation with original contribution to knowledge.

Chapter 2

Theoretical background

2.1 Density-functional theory

2.1.1 Born–Oppenheimer approximation

To derive materials properties from quantum-mechanical level, one should investigate the interactions between nuclei and electrons. This can be accomplished by solving the Schrödinger equation, given as

$$\hat{H}\Psi = E\Psi, \tag{2.1}$$

where $\hat{H}$ is the Hamiltonian, E is the eigenvalues, and Ψ is the corresponding eigenfunctions. Since postulated in 1925, this equation has been laid foundation of *ab initio* calculations. Hamiltonian for the quantum-mechanical system can be written as

$$\begin{aligned}\hat{H} = &-\sum_I \frac{\hbar^2}{2M_I}\nabla_I^2 - \frac{\hbar^2}{2m_e}\sum_i \nabla_i^2 \\ &+ \frac{1}{2}\sum_{I\neq J}\frac{Z_I Z_J e^2}{|\mathbf{R}_I - \mathbf{R}_J|} + \frac{1}{2}\sum_{i\neq j}\frac{e^2}{|\mathbf{r}_i - \mathbf{r}_j|} - \sum_{i,I}\frac{Z_I e^2}{|\mathbf{r}_i - \mathbf{R}_I|},\end{aligned} \tag{2.2}$$

where $\hbar$ and e are the reduced Planck constant and elementary charge, M_I or m_e is the mass of Ith nuclei or electron, Z_I is the atomic number of Ith nuclei, and $\mathbf{R}_I$ or $\mathbf{r}_i$

is the position vector of Ith nuclei or ith electron, respectively. In Eq. 2.2, the first and second terms corresponds to the kinetic energy of nuclei and electrons respectively, the third or fourth terms are Coulomb repulsion between nuclei-nuclei or electron-electron pairs, and the fifth term is nuclei-electron interactions, respectively. Since nuclei are orders of magnitude heavier than electrons, nuclei can be treated as if they are stationary with respect to electrons. Therefore, the motion of electrons can be separated from nuclei. This is called Born-Oppenheimer approximation [20] under which Eq. 2.2 can be reduced to

$$\begin{aligned}\hat{H} &= \hat{T}_e + \hat{V}_e + \hat{V}_{\text{ext}} \\ &= -\frac{\hbar^2}{2m_e}\sum_i \nabla_i^2 + \frac{1}{2}\sum_{i\neq j}\frac{e^2}{|\mathbf{r}_i - \mathbf{r}_j|} + \sum_I V_{\text{ext}}(\mathbf{R}_I),\end{aligned} \tag{2.3}$$

where $\hat{T}_e$, $\hat{V}_e$, and $\hat{V}_{\text{ext}}$ are kinetic energy, electron-electron repulsion, and external potential, respectively, and $V_{\text{ext}}(\mathbf{R}_I)$ is the external potential acting on electrons, exerted from Ith nucleus. However, it is still impractical to directly solve Eq. 2.3 for many-electron systems since there are $3N_e$ degrees of freedom. The density-functional theory introduces more theorems and approximations on the electrons to solve Schrödinger equation, as will be described in the following sections.

2.1.2 Hohenberg–Kohn theorems

The Hohenberg–Kohn theorems [21] consist of two parts. The first theorem states that the external potential $\hat{V}_{\mathrm{ext}}(\mathbf{r})$ is a unique functional of electron density $\rho(\mathbf{r})$. Assuming no degeneracy, this can be proven by starting with the assumption that two external potentials that are different by more than constants, $\hat{V}_{\mathrm{ext}}(\mathbf{r})$ and $\hat{V}'_{\mathrm{ext}}(\mathbf{r})$, give the same ground-state density $\rho(\mathbf{r})$. Since $\hat{T}_e$ and $\hat{V}_e$ in Eq. 2.3 are universal for electrons, those two external potentials produce different Hamiltonian $\hat{H}$ and $\hat{H}'$, respectively; corresponding ground-state wavefunctions, $\Psi(\mathbf{r})$ and $\Psi'(\mathbf{r})$ respectively, are also different but assumed to give the same electron density after integration. Then the ground-state energy of these systems, E and E', satisfies

$$\begin{aligned} E = \langle\Psi|\hat{H}|\Psi\rangle < \langle\Psi'|\hat{H}|\Psi'\rangle &= \langle\Psi'|\hat{H}'|\Psi'\rangle + \langle\Psi'|\hat{H} - \hat{H}'|\Psi'\rangle \\ &= E' + \int [\hat{V}_{\mathrm{ext}}(\mathbf{r}) - \hat{V}'_{\mathrm{ext}}(\mathbf{r})]\rho(\mathbf{r})d\mathbf{r}. \end{aligned} \tag{2.4}$$

The same procedure starting from E' yields

$$E' < E + \int [\hat{V}'_{\mathrm{ext}}(\mathbf{r}) - \hat{V}_{\mathrm{ext}}(\mathbf{r})]\rho(\mathbf{r})d\mathbf{r}. \tag{2.5}$$

A contradiction is found after adding Eqs. 2.4 and 2.5 ($E + E' < E' + E$), so it is concluded that there is no different $\hat{V}_{\mathrm{ext}}(\mathbf{r})$ that gives the same electron density. In other words, there is one-to-one correspondence between $\rho(\mathbf{r})$, Ψ, $\hat{H}$, $\hat{V}_{\mathrm{ext}}$, E, and the other ground-state properties. Then the energy can be expressed as a functional of ground-state density:

$$E[\rho(\mathbf{r})] = \int \rho(\mathbf{r})V_{\mathrm{ext}}(\mathbf{r})d\mathbf{r} + F_{\mathrm{HK}}[\rho(\mathbf{r})], \tag{2.6}$$

where $V_{\mathrm{ext}}(\mathbf{r})$ is the external potential, and

$$F_{\mathrm{HK}}[\rho] = T_e[\rho] + V_e[\rho] \tag{2.7}$$

includes kinetic energy and electron-electron interaction respectively.

The second theorem states that the energy functional (Eq. 2.6) gives its global minimum only when the input density is the ground-state density. If trial density is not the ground state, the energy is also not the global minimum but gives upper bound.

Hohenberg–Kohn theorems therefore indicate the existence of energy functional that depends on the ground-state density. However, there still exist two problems: the input density requires many-body wavefunction, and the actual form of the functional in Eq. 2.6 is unknown. Each is covered in following subsections.

2.1.3 Kohn–Sham equations

Kohn and Sham proposed a (fictitious) single-particle Schrödinger equation that generate the same electron density to the original many-body counterpart [22]. This equation is written as

$$\left(-\frac{\hbar^2}{2m}\nabla^2 + V_{\text{eff}}(\mathbf{r})\right)\phi_i(\mathbf{r}) = \varepsilon_i\phi_i(\mathbf{r}), \tag{2.8}$$

where $V_{\text{eff}}(\mathbf{r})$ is the effective potential, and $\phi_i(\mathbf{r})$ and ε_i are ith Kohn–Sham orbital wavefunctions and energies. The ground-state density is calculated by

$$\rho(\mathbf{r}) = \sum_i^N |\phi_i(\mathbf{r})|^2, \tag{2.9}$$

where N is the number of electrons in the system. In Kohn–Sham density-functional theory, the total energy functional is defined as

$$E[\rho] = T_s[\rho] + \int V_{\text{ext}}(\mathbf{r})\rho(\mathbf{r})d\mathbf{r} + E_{\text{H}}[\rho] + E_{\text{xc}}[\rho], \tag{2.10}$$

where $T_s[\rho]$, $E_{\text{H}}[\rho]$, and $E_{\text{xc}}[\rho]$ are kinetic, Hartree, and exchange-correlation energy of electrons, respectively.

The effective potential in Eq. 2.8 is written as

$$V_{\text{eff}}(\mathbf{r}) = V_{\text{ext}}(\mathbf{r}) + V_{\text{H}}(\mathbf{r}) + V_{\text{xc}}(\mathbf{r}), \tag{2.11}$$

where $V_{\text{H}}(\mathbf{r})$ is the Hartree energy corresponding to the electron-electron Coulomb interaction term, defined as

$$V_{\text{H}}(\mathbf{r}) = e^2\int \frac{\rho(\mathbf{r}')}{|\mathbf{r}-\mathbf{r}'|}d\mathbf{r}', \tag{2.12}$$

and $V_{\text{xc}}(\mathbf{r})$ is the exchange-correlation potential of electrons and defined as

$$V_{\text{xc}}(\mathbf{r}) = \frac{\delta E_{\text{xc}}[\rho]}{\delta\rho(\mathbf{r})}. \tag{2.13}$$

Notably, $E_{\mathrm{xc}}[\rho]$ also contains corrections for the difference between the single-particle orbitals and true electron wavefunctions. While these equations are exact in principle, the exact form of $E_{\mathrm{xc}}(\mathbf{r})$ is unknown in Kohn–Sham density-functional theory. Therefore, the level of approximations for $E_{\mathrm{xc}}(\mathbf{r})$ determines accuracy of the density-functional calculations.

To obtain solutions for Kohn–Sham equation, a trial density $\rho(\mathbf{r})$ is introduced to construct $V_{\mathrm{eff}}(\mathbf{r})$ (Sec. 2.1.2). Then at given $V_{\mathrm{eff}}(\mathbf{r})$, single-orbital wavefunctions $\phi_i(\mathbf{r})$ are obtained after solving the single-particle Schrödinger equation (Eq. 2.8), giving again the electron density $\rho(\mathbf{r})$ (Eq. 2.9) and corresponding energy (Eq. 2.10). These procedures are self-consistent and iterated until reaching the global minimum.

2.1.4 Exchange–correlation functional

To address many-body nature of electrons, approximations have been made for $E_{\rm xc}(\mathbf{r})$ (Eq. 2.13). The simplest one is local density approximation (LDA) [22], where the exchange–correlation energy is functional of electron density at given spatial coordinate. For spin-unpolarized system, it is written as

$$E_{\rm xc}^{\rm LDA}[\rho] = \int \rho(\mathbf{r}) \varepsilon_{\rm xc}^{\rm LDA}[\rho(\mathbf{r})] d^3\mathbf{r}, \tag{2.14}$$

where $\varepsilon_{\rm xc}^{\rm LDA}[\rho(\mathbf{r})]$ is the exchange–correlation energy density within LDA. This is mostly referenced to the homogeneous electron gas, written as

$$E_{\rm xc}^{\rm LDA}[\rho] = E_{\rm x}^{\rm LDA}[\rho] + E_{\rm c}^{\rm LDA}[\rho], \tag{2.15}$$

where

$$E_{\rm x}^{\rm LDA}[\rho] = -\frac{3}{4}\left(\frac{3}{\pi}\right)^{1/3} \int \rho^{4/3}(\mathbf{r}) d\mathbf{r} \tag{2.16}$$

is the exchange energy functional, and $E_{\rm c}^{\rm LDA}[\rho]$ is the correlation energy functional available from quantum Monte Carlo simulations [23]. LDA often works well for systems with uniform electron density.

Since electron densities in solids are non-uniform, corrections are made by gradient of the charge density. This is called generalized-gradient approximation (GGA) and often produce better results than LDA [24]. Its functional form can be expressed as

$$E_{\rm xc}^{\rm GGA}[\rho] = \int \rho(\mathbf{r}) \varepsilon_{\rm xc}^{\rm GGA}[\rho, \nabla\rho] d^3\mathbf{r}, \tag{2.17}$$

where now the energy density $\varepsilon_{\rm xc}^{\rm GGA}$ also depends on the gradient of the electron density $\nabla\rho$. Among various derivatives, the most widely-used GGA functional is the parameterization of Perdew, Burke, and Ernzerhof (PBE) [18]. More recently, the exchange–correlation potential is further modified by kinetic energy of non-interacting orbitals. it is called meta-GGA and written as

$$E_{\rm xc}^{\rm meta-GGA}[\rho] = \int \rho(\mathbf{r}) \varepsilon_{\rm xc}^{\rm meta-GGA}[\rho, \nabla\rho, \tau] d^3\mathbf{r}, \tag{2.18}$$

where τ is the kinetic energy density from Kohn–Sham orbitals. A widely used one is strongly constrained and appropriately normed (SCAN) functional [19], which is benchmarked against PBE and shows decent accuracy over properties of materials and molecules [25].

2.2 Neural network interatomic potential

DFT calculations have been widely used because it can accurately predict physical properties or chemical reactions from interactions between electrons, without empirical parameters. However, since it requires a huge amount of computational resources, attempts to accelerate the DFT calculations by employing surrogate models have been continuing. Recently, models based on machine learning gain much attentions. Among them, Behler [26] proposed neural network interatomic potential (NNP), which is based on feedforward neural network. NNPs are mostly trained on DFT calculations and reproduce them with little computational cost, bypassing the redundant and computationally costly consideration of many-body interactions between electrons.

NNP is a regression model that takes an atomic structure as an input and returns the energy, atomic force, and stress corresponding to the structure. This is schematically presented in Fig. 2.1. While detailed discussions and implementations are provided in Ref. [26, 27], principles and practices are briefly introduced in this section.

2.2.1 Feature vector

If raw Cartesian coordinates of atoms within the structure is used as input features, the model can only predict the energy of structures with the same number of atoms. Instead, by dividing the total energy into the atomic energies, one can predict the total energy from the sum of the atomic energies regardless of the system size. In addition, since the energy of a structure is invariant under rotation or translation of the entire system and under permutation of the same element, it is natural for the input features to satisfy those conditions.

The atom-centered symmetry functions (ACSFs) are proposed by Behler [28], satisfying above-mentioned constraints. This feature vectors encodes the real-space coordinates of the given structures into the atom-wise information about local environments within the certain cutoff radius about the center atom. The ACSFs include 5

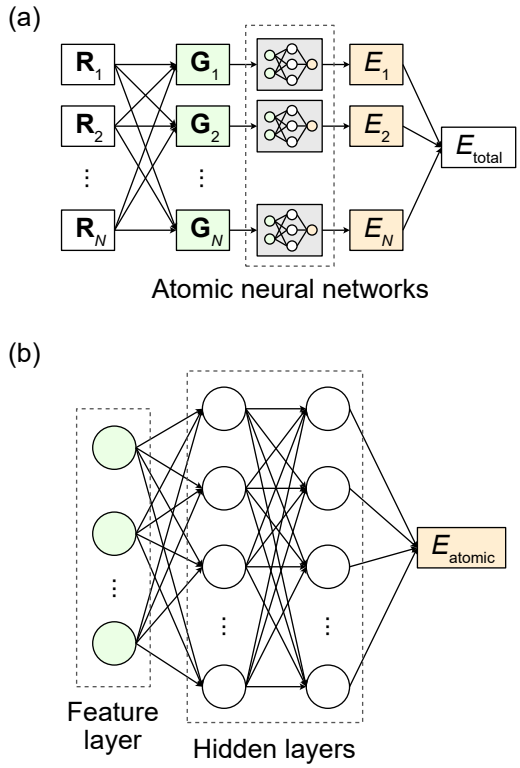

Fig. 2.1: (a) the whole structure of neural network interatomic potential and (b) the atomic neural network. $\mathbf{R}_i$ and $\mathbf{G}_i$ are spatial coordinates and feature vectors of ith atom, respectively. E_i and E_{atomic} indicate atomic energies.

types defined as follows.

$$G_i^1 = \sum_j f_c(R_{ij}), \tag{2.19}$$

$$G_i^2 = \sum_j e^{-\eta(R_{ij}-R_s)^2} f_c(R_{ij}), \tag{2.20}$$

$$G_i^3 = \sum_j \cos(\kappa R_{ij}) f_c(R_{ij}), \tag{2.21}$$

$$G_i^4 = 2^{1-\zeta} \sum_{j,k\neq i}^{all} (1+\lambda\cos\theta_{ijk})^2 e^{-\eta(R_{ij}^2+R_{ik}^2+R_{jk}^2)} f_c(R_{ij}) f_c(R_{ik}) f_c(R_{jk}), \tag{2.22}$$

$$G_i^5 = 2^{1-\zeta} \sum_{j,k\neq i}^{all} (1+\lambda\cos\theta_{ijk})^2 e^{-\eta(R_{ij}^2+R_{ik}^2)} f_c(R_{ij}) f_c(R_{ik}). \tag{2.23}$$

where i, j, and k are atom indices, R_{ij} is the distance between atom i and j, and η, κ, ζ, and λ are hyperparameters that can have multiple values to represent the local environment in detail. G^1, G^2, and G^3 are radial, and G^4 and G^5 is angular functions, respectively. Finally, f_c is the cutoff function that smears out the effect of atoms outside the certain cutoff radius R_c.

$$f_c(R_{ij}) = \begin{cases} 0.5\left[\cos(\pi R_{ij}/R_c)+1\right] & (R_{ij} \leq R_c) \\ 0 & (R_{ij} > R_c). \end{cases} \tag{2.24}$$

The feature vectors have different scale according to the selection of hyperparameters. As the range of input features affects the effective importance of features and thus the performance of final model, they should be scaled to have similar ranges. The most common choice is the `mixmax` scaling, making them have values between 0 to 1.

As seen from the Fig. 2.2, input features are highly correlated to each other, whose dimension is around 100. Thus, instead of using the original features, one may reduce the number of features for accelerating convergence of the training procedure

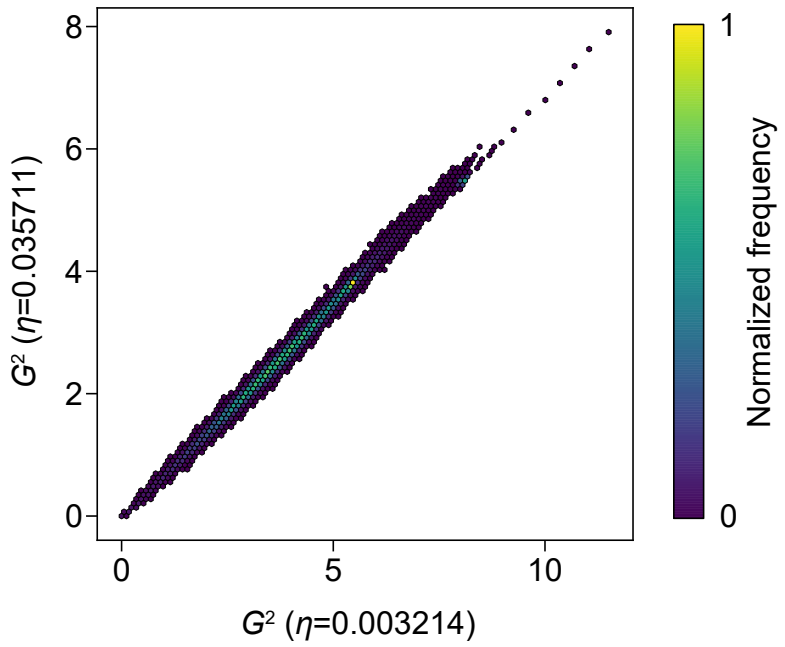

Fig. 2.2: Two atom-centered symmetry functions G^2 (see Eq. 2.20) under different hyperparameters η.

and avoiding overfitting. This can be done by decorrelating these features using, for example, principal component analysis (PCA).

After PCA transformation, the principal components again have different ranges. These are standardized by whitening transformation, making all the values have standard deviation of 1. However, in this case, latter principal axes have orders of magnitude smaller variance than the former axes. Therefore, a minimum whitening level could be selected such that the small-importance principal axes does not act as noises to the model.

2.2.2 Model

The NNP consists of atomic feedforward neural networks that give atomic energies (Fig. 2.1(b)). Beginning from the input layer, nodes and their weights in each layer are connected to the next layer by the analytical relation defined as

$$x_j^{k+1} = f_a \left(\sum_{i=1}^{N^k} x_i^k w_{ij}^k + b^k \right), \tag{2.25}$$

where i (j) is the index of nodes of the kth ($[k+1]$th) layer, w_{ij}^k is the weight connecting the node between x_i^k and x_j^{k+1}, and b^k is the bias of the kth layer. The summation runs for all the nodes in the kth layer (N_k), and f_a is called activation function. While the others are linear arithmetic, the activation function imposes non-linearity to the model. Sigmoid or cotangent functions are common choice for NNPs.

The atomic energies obtained from the atomic neural networks are summed up to give total energy of a given structure. The total energy expression is analytical as given in Eq. 2.25, and the forces can be analytically obtained from the derivative about the Cartesian coordinates, exploiting chain rules.

The regression of the model parameters toward data sets are realized by backpropagation. The NNP is trained by minimizing the loss function (Γ) defined as

$$\Gamma = \frac{1}{M}\sum_{i=1}^{M}\left(\frac{E_i^{\mathrm{DFT}} - E_i^{\mathrm{NNP}}}{N_i}\right)^2 + \frac{\mu_1}{3\sum_{i=1}^{M} N_i}\sum_{i=1}^{M}\sum_{j=1}^{N_i}\left|\mathbf{F}_{ij}^{\mathrm{DFT}} - \mathbf{F}_{ij}^{\mathrm{NNP}}\right|^2 + \frac{\mu_2}{6M}\sum_{i=1}^{M}\sum_{k=1}^{6}\left|S_{ik}^{\mathrm{DFT}} - S_{ik}^{\mathrm{NNP}}\right|^2, \tag{2.26}$$

where M is the total number of structures in the training set, N_i is the number of atoms in the ith structure, and $E_i^{\mathrm{DFT(NNP)}}$, $\mathbf{F}_{ij}^{\mathrm{DFT(NNP)}}$, and $S_{ik}^{\mathrm{DFT(NNP)}}$ are its total energy, atomic force of the jth atom, and the kth component of the virial stress tensor, respectively. μ_1 and μ_2 are the parameters that scale the relative importance of atomic force and stress with respect to the total energy when minimizing the loss function.

As the size of data set becomes large in practices, minimizing the loss function for optimizing network parameters using the whole data set becomes largely inefficient. Stochastic gradient descent, which uses small fractions (batch) of data set to proceed more iterations, can make the training process more computationally efficient. In this process, since the gradient has errors to the true gradient, it is desirable to use information of previous batches. For example, *Adam* (adaptive moment estimation) optimizer is one of the advanced scheme which exploits adaptive step size and momentum.

2.2.3 Data set

The data set should fully span the target simulation domain. This is because the machine learning methods give precise predictions for interpolation but unexpected errors for extrapolation. The conventional approach for constructing data set is based on human intuition and the background knowledge about the system. For example, a data set consists of ground state structures, their strained states, and *ab initio* MD trajectories for the target simulations in small cells. However, data set based only on human intuition and MD simulations may be insufficient. This is because, for example, saddle points of the reaction paths are hardly sampled within Boltzmann statistics in MD simulations.

One of the approaches to overcome the limitation of the conventional approach is augmentation of the data set based on uncertainty prediction. For NNPs, there is no inherent metric for uncertainty, unlike other machine learning methods such as Gaussian process. Instead, one can use the deviations of energy or force within an ensmeble of NNPs [29], which are trained from different random numbers or hidden layer architectures. It would be advantageous for homogeneous system such as bulk or amorphous materials to use uncertainty indicators based on total energy, while inhomogeneous systems including interfaces or chemical reactions require atom-based indicators to resolve the exact source of errors. To accomplish those purposes there are several methods as suggested in Ref. [13]. One can use active learning schemes based on the uncertainty prediction methods to expand the data set toward simulation domain. Starting from the initial data set, the target simulations are repeatedly carried out by NNPs, and the data set is augmented whenever the untrained domain is detected until the simulations becomes stable within the training domain. Other approaches, such as metadynamics have been also suggested to sample a wide range of configurations without human intuition.

The performance of the final model is critically affected by approximations in *ab initio* calculations that are used to construct the data set. When NNPs are trained with DFT calculations, a routine choice is PBE functional. However, when calculating thermal properties, such as phonon dispersion or melting points, it has been repeatedly reported that the PBE functional often gives underestimated phonon frequency or melting points. Instead, the SCAN functional provides more accurate descriptions on a wide range of physical properties and also validated through melting point calculation. Depending on the target simulations, DFT functional that correctly reproduces desired properties should be chosen to obtain reliable results.

Chapter 3

Accelerated computation of lattice thermal conductivity

3.1 Introduction

The prediction of thermal conductivity is of central importance in materials science and engineering for a wide range of applications. For example, materials with low thermal conductivities can be used for thermoelectrics [30] or thermal insulations [31], whereas materials with high thermal conductivities are suitable for the thermal management of electronic devices [32]. In the past decades, the development of *ab initio* methods combined with increasing computational power enabled a reliable prediction of lattice thermal conductivity (κ_l) [30, 33]. This is particularly impressive because the computed κ_l spans a wide range of scales from 10^{-1} to 10^3 $\mathrm{Wm^{-1}K^{-1}}$. However, the *ab initio* evaluation of κ_l becomes expensive in multicomponent or low-symmetry materials due to high computational costs for considering anharmonicity. For instance, the monoclinic β-Ga_2O_3 requires thousands of single-point density- functional theory (DFT) calculations to obtain κ_l. Several approaches that exploit regression techniques have been proposed to save the computational cost, resulting in a significant increase in the computational efficiency [34–36]. One example is the compressive

sensing lattice dynamics method, which uses sparsity in the force constants [34]. In this method, the potential energy surface is Taylor-expanded with the high-order force constants (fourth-order and beyond), which is fitted to DFT atomic forces for reference structures. The temperature-dependent effective-potential method (TDEP) also expands the potential energy surface but the series is usually truncated beyond the third order [35]. Through a fit to *ab initio* molecular dynamics (AIMD) trajectories, the finite-temperature effects of higher-order terms on the force constant and anharmonicity are incorporated in TDEP. Several high-throughput calculations of κ_l have been reported using semi-empirical approaches based on the Debye-Callaway or Leibfried-Schlömann models [37–39]. However, for materials outside of the dataset used to fit the model, κ_l prediction accuracy would deteriorate.

Machine-learned interatomic potentials (MLPs) have recently been used as surrogate models of DFT in calculating force constants and κ_l [40–47]. To fit the potential energy surface produced by *ab initio* calculations, preferably DFT [11], MLPs use flexible regression models. For regression models, artificial neural networks [26], kernel-based methods [48], and linear fitting [49] are popular choices. Once trained, MLPs infer the energy, atomic force, and virial stress of the given structure with an accuracy comparable to DFT, but at a fraction of the cost. Until now, several crystals and alloys have been studied, and κ_l values obtained by MLPs have been close to the reference DFT data. Notably, the κ_l of BAs was successfully predicted by MLP, which demands up to four-phonon scattering in the Boltzmann transport equation [44]. MLPs are also advantageous for investigating the κ_l of disordered phases such as amorphous [46] and liquid systems [45]. For materials dominated by nonperturbative phonon scattering, extensive molecular dynamics (MD) simulations are necessary to get an accurate κ_l, which can be handled efficiently by MLP [47].

Although previous works support that the MLP is a powerful tool in calculating κ_l, several issues need to be addressed. For example, most materials in the previous studies retain high symmetries, three or fewer elements, relatively simple configurations,

and a limited range of κ_l ($>$10 $\mathrm{Wm^{-1}K^{-1}}$). Consequently, it is unclear whether the MLP's prediction accuracy can be maintained for materials in general. Furthermore, recipes for creating the training set differ significantly across the literature, making it difficult to establish a standard approach. Motivated by these observations, we herein investigate the effect of material complexity and different types of training sets on the accuracy and computational cost of κ_l prediction by MLPs. We adopt Behler-Parrinello-type neural network potential (NNP) as an MLP model [26] and consider three types of training sets: i) snapshots of crystals with randomly displaced atoms, ii) AIMD trajectory, and iii) snapshots of crystals with atoms displaced along phonon eigenmodes. Our main goal is to develop a recipe for building a training set that predicts the room-temperature (300 K) κ_l of general bulk materials with high efficiency and reasonable accuracy. The following is how the remaining sections are built: the details of computational methods are described in Sec. 3.2. In Sec.3.3, we conduct a preliminary test on the methods of constructing training sets. In Sec. 3.4, based on the method chosen in the previous test, we calculate κ_l of 25 materials with diverse cell symmetry and a wide range of κ_l values and analyze relative errors and computational efficiencies. We also check the effect of reducing the size of the training set in Sec. 3.5. Finally, we summarize and conclude in Sec. 3.6.

3.2 Computational details

3.2.1 Density-functional theory calculations

All the DFT calculations are performed using Vienna *Ab initio* Simulation Package (`VASP`) [50–52]. The generalized gradient approximation by Perdew–Burke–Ernzerhof (PBE) [18] is used for the exchange-correlation function. The initial structure for each material is obtained from the inorganic crystal structure database (ICSD) [53], which is relaxed further within DFT. The plane-wave cutoff energy and **k**-point grids for the unit-cell optimization are selected such that the energy and atomic forces converge to within 1 meV/atom and 5 meV/Å, respectively. The selected parameters are summarized in Ref. [16]. In addition, the PREC tag is set to "Accurate", and the convergence criteria for the self-consistent cycle is set to 10^{-8} eV. Then, the unit cells are fully optimized including lattice vectors until remaining atomic forces become smaller than 1 meV/Å. The final structure becomes the reference one in generating the training set. The computational parameters used for constructing the training data will be discussed in Sec. 3.3.

3.2.2 Boltzmann transport equation

We calculate the lattice thermal conductivity by solving the phonon Boltzmann transport equation linearized under the relaxation-time approximation. In the following, we briefly summarize the equations involved in computing κ_l. Detailed discussions can be found elsewhere [54, 55]. The potential energy surface U can be expanded as

$$U = U_0 + \frac{1}{2!}\sum_{ij\alpha\beta}\Phi_{ij}^{\alpha\beta}u_i^{\alpha}u_j^{\beta} + \frac{1}{3!}\sum_{ijk\alpha\beta\gamma}\Phi_{ijk}^{\alpha\beta\gamma}u_i^{\alpha}u_j^{\beta}u_k^{\gamma} + ... \tag{3.1}$$

where U_0 is a constant and $\Phi_{ij}^{\alpha\beta}$ and $\Phi_{ijk}^{\alpha\beta\gamma}$ are the second- and third-order interatomic force constants, respectively. u_i is the atomic displacement of the ith atom from the

equilibrium position, and α, β, and γ are the Cartesian indices. At temperature T, the lattice thermal conductivity tensor is expressed as

$$\kappa_{\alpha\beta} = \frac{1}{\Omega} \sum_{\mathbf{q}s} C_{\mathbf{q}s} v^{\alpha}_{\mathbf{q}s} v^{\beta}_{\mathbf{q}s} \tau_{\mathbf{q}s}, \tag{3.2}$$

where Ω is the volume of the crystal and $C_{\mathbf{q}s}$, $v_{\mathbf{q}s}$, and $\tau_{\mathbf{q}s}$ correspond to the heat capacity, phonon velocity, and phonon lifetime with the wave vector $\mathbf{q}$ and branch index s, respectively. In Eq. 3.2, the heat capacity is defined as

$$C_{\mathbf{q}s} = \hbar\omega_{\mathbf{q}s} \frac{\partial n_{\mathbf{q}s}}{\partial T}, \tag{3.3}$$

where $\hbar$ is the reduced Planck constant, $\omega_{\mathbf{q}s}$ is the angular frequency of the phonon mode $\mathbf{q}s$, and $n_{\mathbf{q}s}$ is the Bose–Einstein occupation number at temperature T. The phonon lifetime is calculated as the inverse of the total scattering rate

$$\frac{1}{\tau_\lambda} = \sum_{\lambda'\lambda''}^{+} \Gamma^{+}_{\lambda\lambda'\lambda''} + \frac{1}{2} \sum_{\lambda'\lambda''}^{-} \Gamma^{-}_{\lambda\lambda'\lambda''} + \sum_{\lambda'} \Gamma_{\lambda\lambda'} \tag{3.4}$$

where Γ^{+} and Γ^{-} are three-phonon scattering rates, corresponding to absorption and emission processes, respectively. Here the phonon mode $\mathbf{q}s$ is abbreviated to a single index λ. The last term on the right-hand side of Eq. 3.4 corresponds to scattering by isotopes present in nature. The three-phonon scattering rates Γ^{+} and Γ^{-} are expressed as

$$\Gamma^{+}_{\lambda\lambda'\lambda''} = \frac{\hbar\pi}{4} \frac{(n_{\lambda'} - n_{\lambda''})}{\omega_\lambda \omega_{\lambda'} \omega_{\lambda''}} \left|V^{+}_{\lambda\lambda'\lambda''}\right|^2 \delta\left(\omega_\lambda + \omega_{\lambda'} - \omega_{\lambda''}\right), \tag{3.5}$$

$$\Gamma^{-}_{\lambda\lambda'\lambda''} = \frac{\hbar\pi}{4} \frac{(n_{\lambda'} + n_{\lambda''} + 1)}{\omega_\lambda \omega_{\lambda'} \omega_{\lambda''}} \left|V^{-}_{\lambda\lambda'\lambda''}\right|^2 \delta\left(\omega_\lambda - \omega_{\lambda'} - \omega_{\lambda''}\right). \tag{3.6}$$

In Eqs. 3.5 and 3.6, the Dirac delta functions δ impose the energy conservation during scattering. The scattering matrix elements $V^{\pm}_{\lambda\lambda'\lambda''}$ are computed as

$$V^{\pm}_{\lambda\lambda'\lambda''} = \sum_{i,j,k} \sum_{\alpha\beta\gamma} \Phi^{\alpha\beta\gamma}_{ijk} \frac{\mathbf{e}^{\alpha}_{i}(\lambda) \mathbf{e}^{\beta}_{j}(\pm\lambda') \mathbf{e}^{\gamma}_{k}(-\lambda'')}{\sqrt{M_i M_j M_k}}, \tag{3.7}$$

where $\mathbf{e}_i(\lambda)$ and M_i are normalized eigenvectors of mode λ and the atomic mass of the ith atom, respectively. Here $-\lambda$ refers to the phonon mode in the wave vector $-\mathbf{q}$ and branch s. Finally, the summation index i and indices j and k in Eq. 3.7 indicate atoms in the unit cell and supercell, respectively.

The second-order interatomic force constants $\Phi_{ij}^{\alpha\beta}$ in Eq. 3.1 are calculated with a finite displacement method using the `Phonopy` package [56]. The side lengths of supercells used in the computation are $\sim$20 Å each. The third-order interatomic force constants ($\Phi_{ijk}^{\alpha\beta\gamma}$ in Eq. 3.1), also calculated with a finite displacement method, and lattice thermal conductivities at 300 K are evaluated by the `ShengBTE` package [54]. Here the supercell dimension is typically $\sim$10 Å with $\sim$6 Å for the cutoff radii of the interatomic interaction. The number of single-point force calculations increases with the number of possible atomic pairs in the supercell, considering the cutoff radii of the interatomic interaction. For the $\mathbf{q}$-point sampling, a uniform mesh grid with a density of $\sim$19 points Å^{-1} is used. The Dirac delta functions in Eqs. 3.5 and 3.6 are approximated by the adaptive Gaussian with a proportionality factor of 0.1 [54]. Under the relaxation time approximation, the Boltzmann transport equation is not solved iteratively. Because the current work focuses on comparing the results of DFT and NNP, we do not consider nonanalytic corrections for LO–TO splitting. The full details on the computational parameters used to evaluate force constants can be found in Ref. [16].

3.2.3 Neural network potential

For training NNPs, we employ the `SIMPLE-NN` package [27]. Atom-centered symmetry functions G^2 and G^4 [28] are adopted to describe radial and angular distributions of neighboring atoms, respectively. The cutoff radius is set to 6.5 Å, and 26, 70, and 132 symmetry functions are employed for unary, binary, and ternary systems, respectively. The network architecture comprises two hidden layers with 60 hidden nodes each and one output layer that provides atomic energy. The input vector is decorrelated by principal component analysis and then whitened to increase the learning speed [5]. We set

the parameters μ_1 and μ_2 in the loss function (Eq. 2.26), scaling the relative importance of atomic force and stress with respect to the total energy, as 10^2 and 10^{-6}, respectively. To avoid overfitting and obtain more regularized NNPs, we apply a dropout technique in which half of the nodes are randomly selected and fixed at each training iteration [57]. The learning rate starts at 0.01 and scales by 0.1 every 5000 iterations. We train two independent NNPs and use averaged forces to obtain interatomic force constants for given atomic displacements. For evaluating atomic forces, we use the `LAMMPS` package [58].

3.3 Construction of training sets

To select an optimal approach to generate training sets, preliminary tests are conducted on six materials: BAs, $CoSb_3$, β-Ga_2O_3, GaP, α-SiO_2, and Tl_9BiTe_6 that span three orders of κ_l from 10^{-1} to 10^2 $Wm^{-1}K^{-1}$. We compare the three methods of constructing the training set: (i) random displacements of atoms (RDA), (ii) AIMD, and (iii) superposition of phonon eigenmodes (SPE). Each atom is displaced with random directions and amplitudes in the RDA method. The amplitudes are chosen from a normal distribution with a standard deviation of 0.1 Å. The AIMD method comprises two steps. First, the AIMD using an NVT ensemble is conducted over 1 ps with the time step of 1 fs, at temperatures of 50, 300, 500, and 700 K, following the choice of the simulation time and temperatures in Ref. [42]. (We also tested the AIMD method with NPT ensemble, but the resulting κ_l showed no significant difference.) The simulation cell, which contains $\sim$100 atoms, is identical to the one used to calculate the third-order interatomic force constants for the most cases of the test materials. During AIMD, the computational parameters are slightly loosened such that the self-consistency criteria is set to 10^{-4} eV with the default plane-wave energy cutoff and the Γ-point sampling. Next, we sample the 4-ps AIMD trajectories in 10- or 80-fs intervals depending on the target size of the training set, and more accurate DFT calculations are performed on the sampled structures. This is required because the interatomic force constants are sensitive to computational precision, so the training data must maintain high precision. In these calculations, the plane-wave energy cutoff, **k**-point grids, and convergence criteria of self-consistent calculation are set to the same as those of the unit cell optimization (see Section 3.2.1). Finally, the SPE method requires the second-order interatomic force constants that determine the phonon eigenmodes. To roughly calculate the second-order interatomic force constants with minimal computational costs, we use the Γ point and a small supercell size adopted in calculating third-order interatomic force constants (see Section 3.2.1). Each atom is displaced along the superposed phonon

modes with random amplitudes and phase factors [36].

In each of the three approaches described above, the training set comprises 400 structures. To calculate third-order interatomic force constants, interactions up to $\sim$6 Å or 6th, 7th, 19th, 5th, 11th, and 4th nearest neighbors are considered for BAs, $CoSb_3$, β-Ga_2O_3, GaP, α-SiO_2, and Tl_9BiTe_6, respectively. For the phonon dispersion, every NNP trained by the three methods reproduces phonon dispersion for all six materials [16]. Figures 3.1(a)–(c) present the comparisons of the diagonal components of the κ_l tensor between NNP and DFT. We also compare the DFT results with experimental data in Fig. 3.1(d) to validate computational settings. It is seen that NNP-AIMD shows higher accuracy than other methods, with the error bound for all test materials being less than 30%. Conversely, NNP-RDA and NNP-SPE show error levels larger than a factor of 2 for GaP and β-Ga_2O_3, respectively. This means that RDA and SPE method may produce atomic displacements that have no bearing on third-order interatomic force constants. Since the RDA method does not make any assumptions about atomic correlations, it is more likely to produce unphysical atomic configurations with small interatomic distances and large repulsive atomic forces. This analysis is supported by the phonon scattering rates of GaP shown in Fig. 3.2; while NNP-AIMD shows good accuracy in predicting frequency-scattering rates relations, the other two NNPs show large discrepancies, especially NNP-RDA.

The computational cost of the SPE method varies greatly depending on the cell symmetry due to the part on obtaining phonon dispersion. The costs of the AIMD and RDA methods, however, are less affected by crystal symmetry. Consequently, we conclude that the AIMD method is the best for generating training data. In passing, we note that for BAs, the present DFT result of κ_l ($\sim$1200) in Fig. 3.1 deviates from the previous literature ($>$2000) [42]. This is because we did not solve the Boltzmann transport equation iteratively (i.e., relaxation time approximation), which is known to affect the prediction accuracy for materials with high κ_l [54]. When the Boltzmann transport equation is solved iteratively, we find that κ_l increases to $\sim$1900.

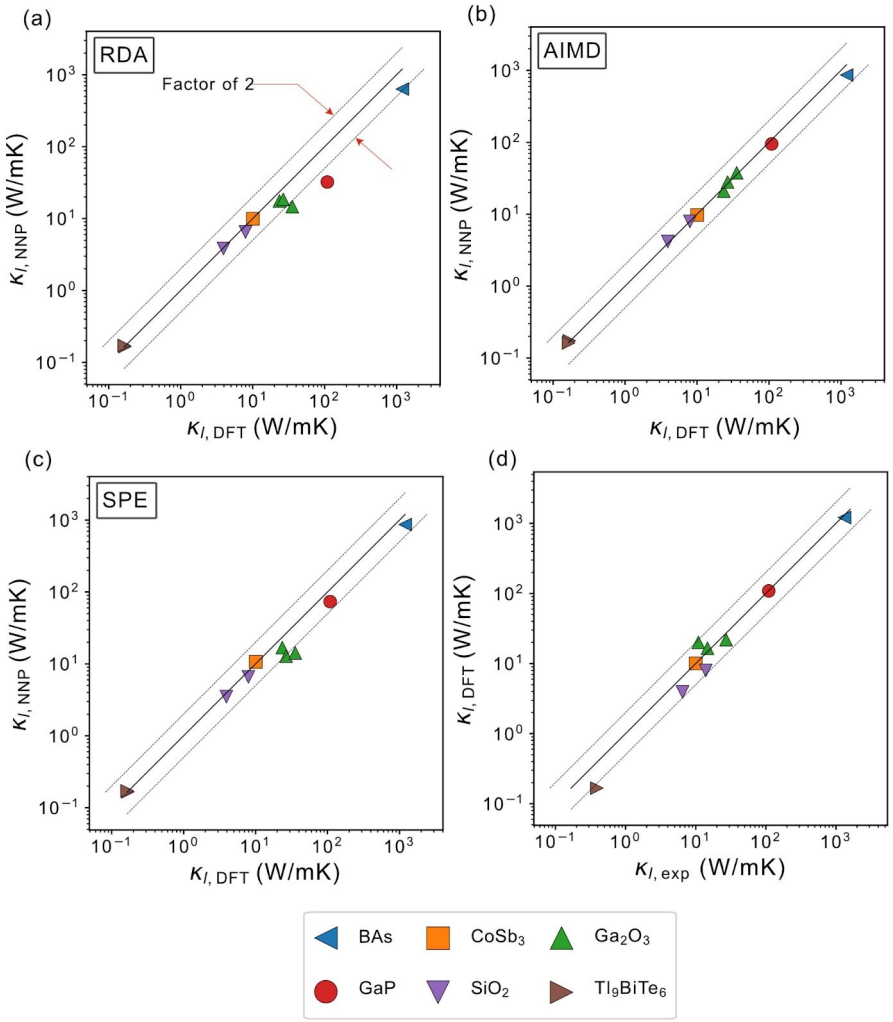

Fig. 3.1: κ_l of test materials calculated by density-functional theory (DFT) and neural network potentials (NNPs) that are generated with various training sets. (a) Random displacements of atoms (RDA), (b) ab initio molecular dynamics (AIMD), (c) superposition of phonon eigenmodes (SPE). (d) Comparison between DFT and experimental values. Multiple values for each symbol denote the diagonal components of κ_l, and gray lines denote the error with a factor of 2. The data for experimental κ_l values are referred to the original publication and the references therein [16].

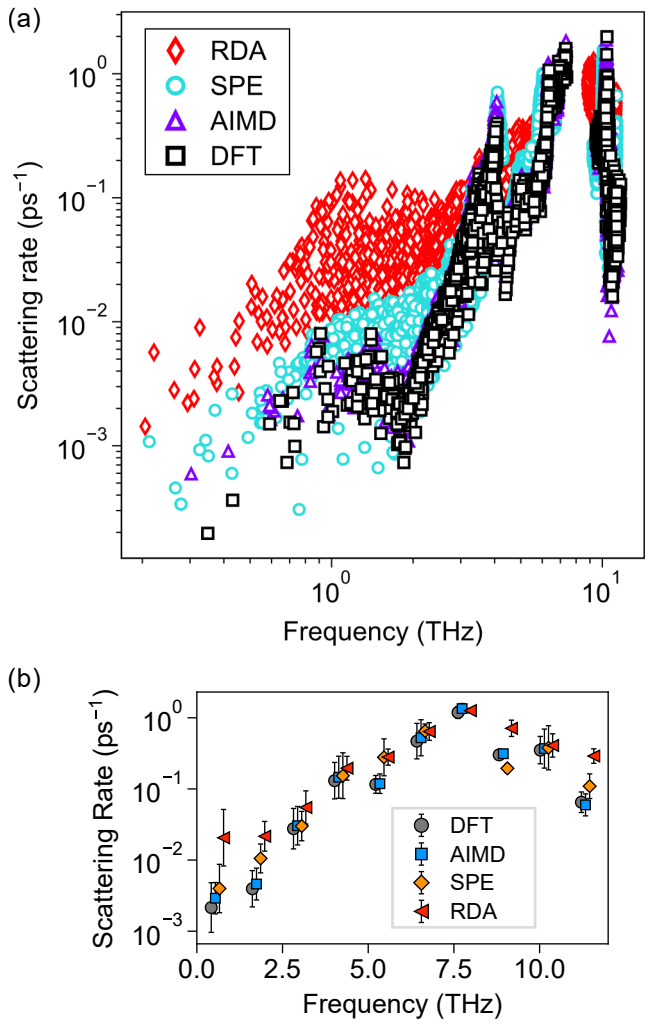

Fig. 3.2: The frequency-dependent phonon scattering rates of GaP obtained by DFT and NNPs (a), averaged over every 1.2 THz intervals (b). Error bars in (b) indicate standard deviation within the interval [16].

3.4 Computation of κ_l for diverse materials

This section increases the benchmark cases to 25 materials with diverse cell symmetries and a wide range of κ_l values. The training set for each NNP comprises 400 structures generated by the AIMD method. Figure 3.3(a) compares κ_l between NNP-AIMD and DFT. The root-mean-squared relative error (RMSRE) of test materials is 18.6%. To be more informative, results of three materials with different symmetry are provided in Fig. 3.5, showing good agreements with DFT calculations in phonon dispersion, scattering rate, and κ_l. Figure 3.3(b) shows the results when the training data is reduced, as discussed below. For comparison, we gather the κ_l values computed by MLP and DFT from the literature and plot them in Fig. 3.4(a) (For a fair comparison, only those obtained by solving the Boltzmann transport equation are presented). Except for a few materials, the error level in Fig. 3.3(a) and Fig. 3.4(a) is similar. Figure 3.4(b) explicitly compares the error values for common materials in Fig. 3.3(a) and Fig. 3.4(b). It can be seen that the errors from the present approach are comparable to those of other references even though we use a consistent choice of the training set. However, BAs shows a much larger error than Ref. [44]. It is known that κ_l of BAs is mainly determined by the scattering of acoustic phonon modes. Ref. [44] employed NPT simulations and adopted DFT results for the harmonic part, which may have contributed to more accurate scatterings by acoustic phonons.

We note that materials with low symmetries often exhibit large errors in Fig. 3.3(a). To be specific, we classify the test materials into four groups based on the crystal system: (1) cubic, (2) tetragonal and hexagonal, (3) orthorhombic, and (4) monoclinic and triclinic. For each material, we first select the component of κ_l showing the largest error. For the selected components, we calculate the average error within each group. The results are 7.6%, 13.5%, 15.7%, and 24.2% for the group (1)–(4), respectively, which shows a trend of increasing errors with low crystal symmetries. The low symmetry may require longer AIMD simulations for sufficient sampling. To test this, we

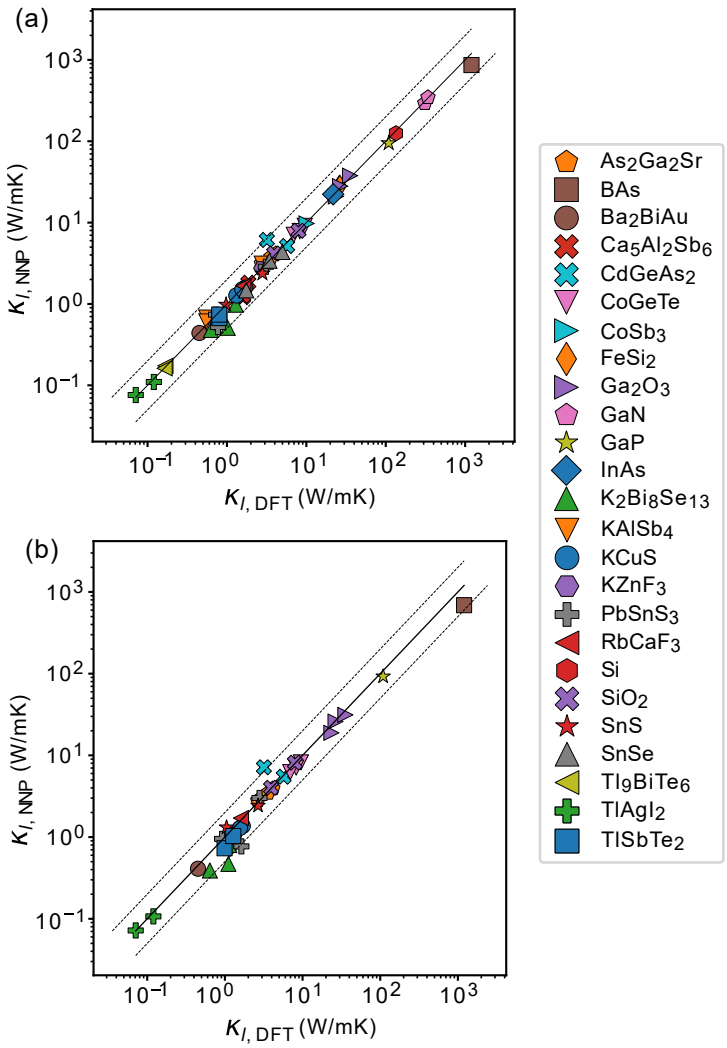

Fig. 3.3: κ_l computed by NNP-AIMD trained with (a) 400 and (b) 50 structures sampled from the same AIMD trajectories [16].

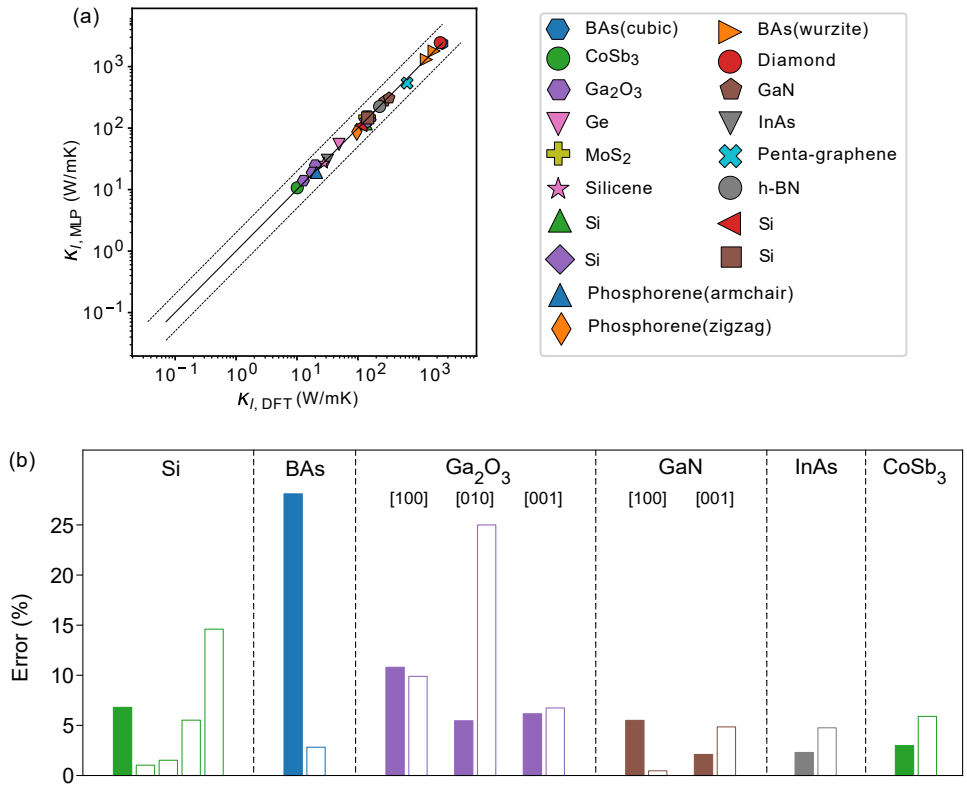

Fig. 3.4: (a) DFT and machine-learned potentials (MLP) results quoted from literature. (b) Comparison of errors in κ_l prediction by MLPs for the materials common in Fig. 3.3. The filled and empty bars are the present results and references, respectively. The exact sources are referred to the original publication and the references therein [16].

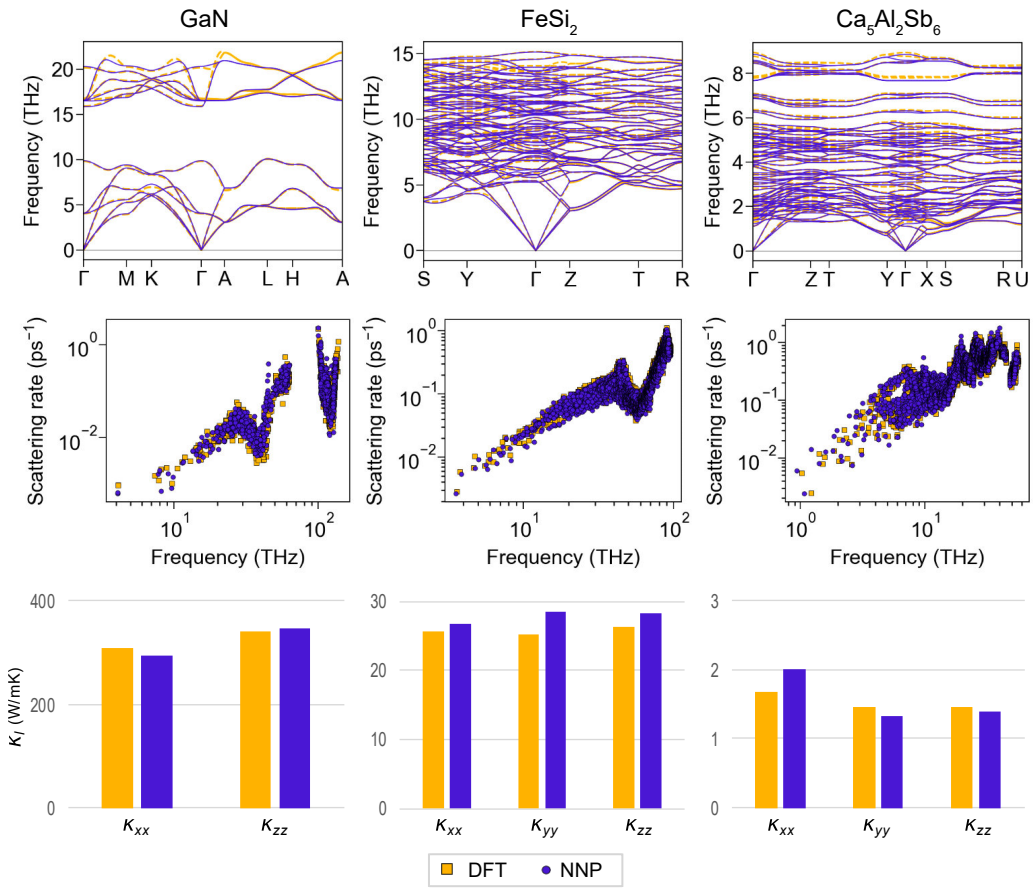

Fig. 3.5: Phonon dispersion, scattering rate, and lattice thermal conductivity of GaN, $FeSi_2$, and $Ca_5Al_2Sb_6$.

extend AIMD of $K_2Bi_8Se_{13}$, which has $P\bar{1}$ space group and thus has the largest error, up to 2 ps, increasing the training set by two folds. However, the resulting NNP for $K_2Bi_8Se_{13}$ produces almost identical κ_l. Therefore, the origin of the error and a systematic solution need further investigation in future.

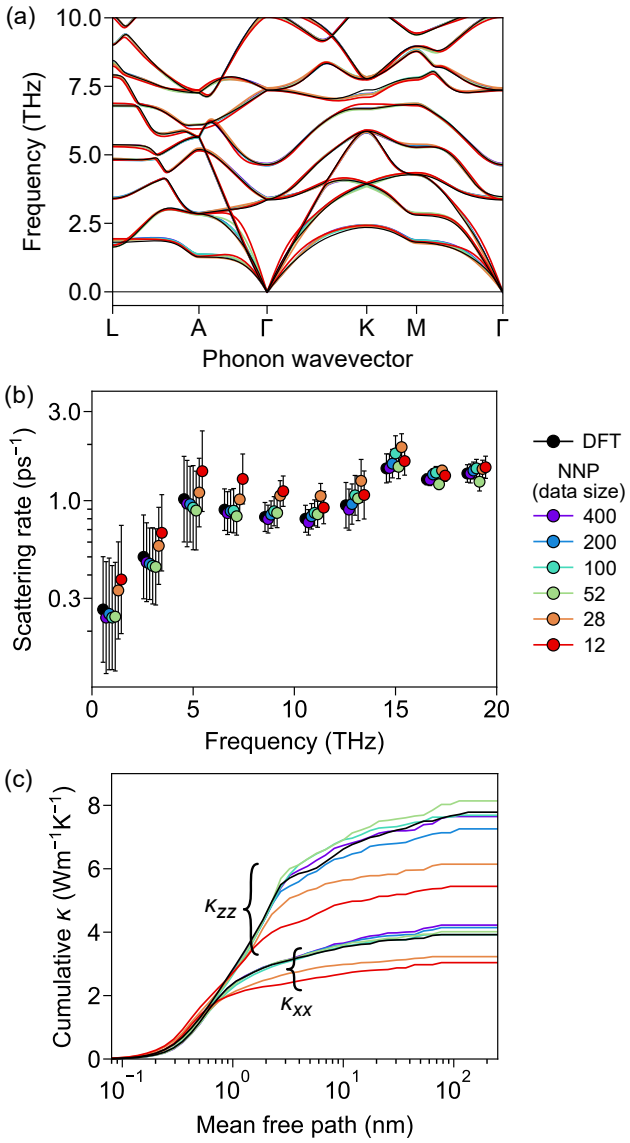

Fig. 3.6: Data-size dependence of (a) phonon dispersion, (b) scattering rate, and (c) cumulative lattice thermal conductivity as a function of the phonon mean free path. The phonon dispersion is presented up to 10 THz for clarity. Scattering rates are averaged over every 2 THz intervals, and error bars indicate standard deviation within the interval [16].

3.5 Savings on computational cost

The high-precision DFT calculations used to construct the training set account for about 90% of the computational costs in the present work. The other portions of the computational cost stem from AIMD, NNP training, and κ_l calculation, with each corresponding to $\sim$3 % respectively. Consequently, it would be worthwhile to see if the training set could be shrunk further to save on computational costs. To this end, we investigate the effect of dataset size on κ_l using αSiO_2 as an example. First, we choose 12, 28, 52, 100, 200, and 400 structures from 108-atom AIMD data, which train six different NNPs. The simulation time and temperatures are the same as those in the previous section. In Fig. 3.6, we calculate phonon dispersions, scattering rates, and cumulative lattice thermal conductivities as a function of the phonon mean free path. Figure 3.6(a) shows that harmonic properties are well described by every NNP, but a slight deviation of the transverse acoustic mode is observed along the Γ–A line with the data size of 12. The scattering rates and cumulative κ_l in Figs. 3.6(b) and 3.6(c), respectively, are well reproduced for data sizes exceeding 28. With data sizes of 12 or 28, significant deviations in κ_l are observed mostly at mean free paths of 1–10 nm.

Following the above analysis, we reduce the training set to 50 structures for 18 materials selected from Fig. 3.3(a) by sampling more sparsely over the same MD trajectories. The κ_l values compared between the resulting NNPs and DFT are shown in Fig. 3.3(b). The RMSRE of the κ_l is 31%, increasing from 18% in Fig. 3.3(a), which is reasonable considering the drastic decrease in computational cost. Again, $K_2Bi_8Se_{13}$ shows the largest error as in Fig. 3.3(a), which can be understood by the low symmetry in the crystal structure.

Additionally, we analyze the computational efficiency of the NNP-based calculation of κ_l with respect to the DFT-based calculation. Figure 3.7 shows how the computational cost changes as the material complexity increases. The number of structures required to calculate the third-order force constants, which encompasses the number

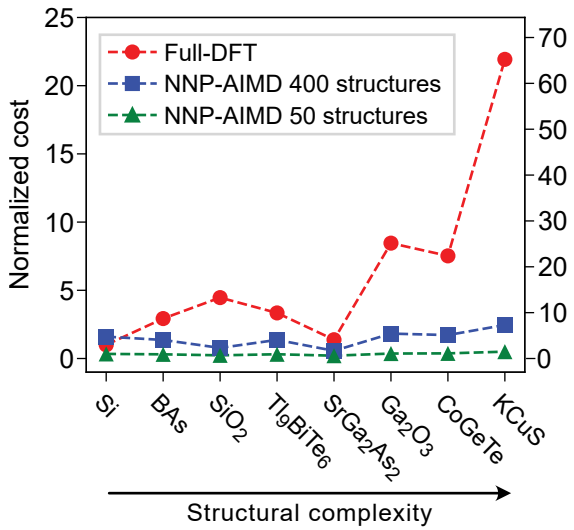

Fig. 3.7: The computational cost of calculating κ_l by DFT and NNPs trained by 400 or 50 structures. The computational cost is normalized with respect to Si computed within the fully DFT approach (left scale) or the NNP trained with 50 structures (right scale) [16].

of atomic elements, the number of atoms in the unit cell, and the crystal symmetry, is used to rank the material complexity. The computational cost is normalized with respect to that of Si computed using the full DFT approach (left scale) or the NNP trained with 50 structures. (right scale). Here, the computational cost of the DFT-based κ_l calculation is the summation of those obtaining second- and third-order force constants. The majority of the computational costs in NNP-based calculations come from building the training set (AIMD and single-shot calculations) and training NNPs, while the cost of calculating force constants using the finite displacement method is negligible. As the material complexity increases, the number of structures needed to generate the third-order force constants increases rapidly, which is confirmed in Fig. 3.7. For instance, the DFT computational cost for KCuS is more than 20 times higher than that of Si. Conversely, NNP-based κ_l calculations show nearly constant computational costs regardless of the material complexity. This is because the cost of AIMD and high-precision DFT calculations are similar among the materials. This is because the atomic forces can be calculated with almost no cost once the NNP has been trained, even for a very large supercell.

3.6 Summary

In summary, we propose a standard protocol for building the training set of NNPs targeted for computing κ_l efficiently without fine-tuning for each material. The protocol requires 1-ps AIMD simulations at various temperatures and accurate single-shot calculations for 400 structures sampled along the MD trajectory. Testing over 25 materials with diverse symmetries and wide range of κ_l, it is confirmed that NNP-AIMD provides consistent accuracies comparable to reported values in the literature. The uniform cost across material types for the proposed method makes it especially efficient for complex materials whose κ_l prediction would be costly in a full-DFT approach. Furthermore, the NNPs showed reasonable accuracy even when the training set was reduced to 50 structures. Having confirmed that the machine-learned potential reproduces well the anharmonicity, which is a prerequisite for predicting high-temperature properties, the next Chapter will extend its application range to melting properties and phase diagrams.

Chapter 4

Ab initio construction of MgO–CaO full phase diagram

4.1 Introduction

By informing phase formation under the given temperature, pressure, or composition, the phase diagram plays an important role in designing and processing materials [59, 60]. However, determination of the phase diagram requires a huge amount of experimental efforts, particularly for multicomponent systems [61, 62]. This is because while possible combinations of temperature and composition are vast, each data point becomes only reliable with consistent observations from complementary techniques. As such, full phase diagrams are sparse for multicomponent systems [61].

Theoretically, the phase diagram is determined by the Gibbs free energies of competing phases, where the lowest ones appear in the equilibrium phase diagram. Several computational methods based on molecular dynamics (MD) have been developed for computing the free energies from atomistic simulations: thermodynamic integration, coexistence method, and semigrand ensemble [63–67]. Among these methods, the coexistence method allows the calculation of the free energy difference between the two phases by directly simulating the equilibrium of a large-scale simulation cell containing those phases and interfaces [65, 66]. On the other hand, the absolute free energy can be computed by the thermodynamic integration method without direct evaluation

of the partition function, which is applicable for pure solids or liquids but not for solid solutions [63, 65]. The free energy of such mixtures can be determined by calculating derivatives of the free energy about composition using a semigrand ensemble and integrating them from the pure phases [63, 67]. By exploiting those complementary methods, one can calculate the composition-dependent free energy for any systems.

In combination with the density-functional theory (DFT), these methods allow for evaluating free energies without experimental inputs. For example, various single-component phase diagrams including melting properties have been constructed by employing the above-mentioned methods [68–74]. However, in binary or higher-order systems, the MD-based approaches are limited with DFT because the sampling over compositional variations and configurations requires iterative simulations over millions of time steps and large simulation cells containing hundreds of atoms [75, 76]. Alternatively, the MD-free cluster expansion was employed in constructing phase diagrams of solid alloys by interpolating free energies of alloy configurations [63, 77–83]. However, this approach is applicable to only crystal systems, and its accuracy degrades when atomic relaxations are significant [84]. Ideal solution approaches were also employed along with special quasi-random structures [85] to approximate the mixture with a single configuration.

In recent years, machine-learned potentials (MLPs) have gained much attention as they can provide energies with near-DFT accuracy at a fraction of the cost [11]. The computational acceleration using MLPs has been confirmed over a wide range of applications including, for example, crystal structure prediction [14] and lattice thermal conductivity [16]. In addition, MLPs are suitable as surrogate models of DFT in evaluating free energies, which has been successfully demonstrated in many recent studies. [40, 86–98] However, examples are mostly single-component systems [40, 86–95] and only a few examples, $\mathrm{Ag}_x\mathrm{Pd}_{1-x}$ [96], $\mathrm{Ni}_x\mathrm{Mo}_{1-x}$ [97], and $\mathrm{Ga}_x\mathrm{As}_{1-x}$ [98], have been attempted for constructing the phase diagram of compounds. Therefore, the accuracy and efficiency of MLPs for constructing the whole phase diagram of multi-

component systems are yet to be confirmed. With these motivations, herein we aim to construct a full temperature-composition phase diagram for the MgO-CaO, an archetypal pseudo-binary system with rich experimental information, using Behler-Parrinello-type neural network potentials (NNPs) [26].

Our strategy for computing the free energy and constructing the phase diagram is as follows: first, for pure phases, temperature-dependent free energies are calculated using the thermodynamic integration method. For pure MgO and CaO, we consider rocksalt and liquid phases, and the crossing of the free energy curves of both phases corresponds to the melting point. Next, the composition-dependent free energy of mixing is calculated using semigrand ensemble simulations at selected temperatures. Since no intermetallic compound exists along the MgO-CaO pseudo-binary line, only the rocksalt solid solution phase and liquid mixture are considered. The above two methods are complementary: the thermodynamic integration method computes the absolute free energy but is limited to a fixed composition, making this method optimal to pure phases. On the other hand, the semigrand ensemble method computes the composition-dependent derivative of free energy that can be integrated from the pure phase. The whole temperature- and composition-dependent free energies are fitted into analytical forms, and phase boundaries are determined by common tangents on the isothermal sections of free energy curves. The rest of the paper is organized as follows: in Sec. 4.2 we introduce computational methods used in the present work such as NNPs, thermodynamic integration, and semigrand ensemble simulations. The main results are discussed in Sec. 4.3 and 4.4, and Sec. 4.5 summarizes this Chapter.

4.2 Theoretical methods

4.2.1 Neural network potential and DFT calculations

In the present work, the Behler-Parrinello-type NNPs [26] are trained by using the `SIMPLE-NN` package [27, 99]. For input features, we use atom-centered symmetry functions (ACSFs) [28]. The numbers of features are 24 and 108 for the radial and angular parts, respectively, with cutoff radii of 7.0 and 4.5 Å, respectively. Since three-body interactions require more computational resources than two-body interactions, we tune the angular cutoff to accelerate the MD simulations. When compared to the single cutoff of 7 Å, we confirm that 10x speed gain can be obtained with negligible compromise in accuracy, as will be validated in Sec. 4.3. The full parameters for ACSFs are listed in Ref. [17]. The training is accelerated by decorrelating features using principal component analysis and whitening [5]. We use an initial learning rate of 0.01, which decays exponentially during 190 epochs and becomes 0.0005 at the final epoch. We use a fully connected atomic neural network with two 60-node hidden layers. The MD simulations and evaluations of energy, force, and stress are carried out using the `LAMMPS` package [27, 58].

The DFT calculations for the training set are carried out using Vienna *Ab initio* Simulation Package (`VASP`) [50–52] with the projector-augmented wave pseudopotentials [100]. The pseudopotential contains the valence electrons of $3s^2$, $3s^2 3p^6 4s^2$, and $2s^2 2p^4$ for Mg, Ca, and O, respectively. We generate data sets independently using two types of the exchange-correlation functional; the widely-used the generalized gradient approximation (GGA) by Perdew-Burke-Ernzerhof (PBE) [18] and strongly constrained and appropriately normed (SCAN) meta-GGA functional [19]. The SCAN functional has been benchmarked against PBE on diverse properties, providing more accurate lattice parameters [19], formation enthalpies [25], lattice dynamics [101], energies of metastable phases [102], and the melting points [93, 103]. For *ab initio* MD simulations, we use default plane-wave energy cutoffs with the Γ-point sampling for

the Brillouin zone integration. Then more accurate DFT calculations are performed on selected snapshots for reference data set by increasing the plane-wave energy cutoff to 500 eV and employing 3×3×3 **k**-point meshes for the conventional unit cell of rock-salt MgO and CaO, which is scaled in supercells to select a similar **k**-point density. Details on the training structures will be discussed in Sec. 4.3.1.

4.2.2 Thermodynamic integration

Thermodynamic integration allows one to calculate the free energy by computing the work done in the isothermal switching process from a reference state whose free energy is known *a priori*, to a state of interest [64, 65, 71, 104]. We apply this method for pure rocksalt and liquid phases of MgO and CaO. When the potential energy term of Hamiltonian of the reference system (U_{i}) and of the system of interest (U_{f}) is given, a parametric potential is defined as

$$U(\lambda) = (1-\lambda)U_{\mathrm{i}} + \lambda U_{\mathrm{f}}, \tag{4.1}$$

where λ is a coupling parameter ranging from 0 to 1. The difference in the Helmholtz free energy between the two systems ($F_{\mathrm{f}} - F_{\mathrm{i}}$) is given by

$$F_{\mathrm{f}} - F_{\mathrm{i}} = \int_0^1 \left\langle \frac{\partial U(\lambda)}{\partial \lambda} \right\rangle_\lambda d\lambda, \tag{4.2}$$

where the $\langle .. \rangle_\lambda$ denotes the ensemble average under the NVT condition at constant λ, which is practically replaced by a temporal average according to the ergodicity.

We employ two reference systems depending on the final state: the Einstein crystal for solid phases and Lennard-Jones (LJ) fluid for liquid phases. The free energy of Einstein crystal is given by

$$F = \sum_i 3n_i k_{\mathrm{B}} T \ln\left(\frac{h\omega_i}{2\pi k_{\mathrm{B}} T}\right), \tag{4.3}$$

where k_{B}, h, and T mean the Boltzmann constant, Planck constant, and temperature, respectively, and n_i and ω_i correspond to the number of atoms and angular frequency

of Einstein oscillators of atomic species i, respectively. We use a spring constant of 5 eV/Å^2 throughout this work regardless of atomic species.

For the liquid phase, we select for the reference system the "cut and shifted" LJ potential [105]. In Ref. [105], the residual free energy of the LJ fluid in reference to the ideal gas was parameterized into an equation of state, which provides highly accurate free energies over a wide range of temperatures and densities. The free energy of the ideal gas is given by

$$F = -k_{\mathrm{B}}T \sum_i \ln\left(\frac{V^{n_i}}{\Lambda_i^{3n_i} n_i!}\right), \tag{4.4}$$

$$\Lambda_i = \frac{h}{\sqrt{2\pi m_i k_{\mathrm{B}} T}}, \tag{4.5}$$

where V is the volume of the system and Λ_i is the thermal De Broglie wavelength of the atomic species i with the atomic mass of m_i. To avoid a phase transition along the integration path, the depth of the LJ potential is controlled such that the LJ fluid becomes supercritical, and the diameter of LJ particles is chosen to have a nearest-neighbor distance similar to the final state [65].

4.2.3 Semigrand ensemble siumlations

Taking the example of a binary system made of atoms A and B, the difference of chemical potentials is written as

$$\Delta\mu(x,T) \equiv \mu_{\mathrm{B}}(x,T) - \mu_{\mathrm{A}}(x,T) = \frac{\partial G(x,T)}{\partial x}, \tag{4.6}$$

where x is the mole fraction of species B and G is the Gibbs free energy. $\Delta\mu(x,T)$ can be obtained by the semigrand ensemble, a subset of the grand-canonical ensemble in which the number of atoms is fixed but chemical identities can change freely [67, 75, 76, 106]. In practice, the equilibration within the semigrand ensemble is achieved by hybridizing MD simulations with Monte Carlo (MC) swap of atomic species. The MC particle swap is accepted by the Metropolis criterion defined as

$$p = \min\left[1, \exp\left\{\left(-\frac{\Delta E - \Delta\mu N \Delta x}{k_{\mathrm{B}}T}\right)\right\}\right], \tag{4.7}$$

where ΔE and Δx indicate the change of energy and composition of the simulation cell due to the test flipping of atomic species respectively, and N is the total number of atoms [106]. After sufficient MD-MC runs, the equilibrium composition x is obtained for the given $\Delta\mu$. By iterating the semigrand ensemble simulations over a range of $\Delta\mu$, $x(\Delta\mu)$ and its inverse $\Delta\mu(x)$ are obtained at given T, and the free energy $G(x,T)$ is obtained in turn by integrating Eq. 4.6. A more formal derivation [67], practical implementation [106], and application examples [75, 76] of the semigrand ensemble are referred to the literature. During the MD simulations, the isobaric condition is imposed to consider composition-dependent of lattice parameters.

4.3 Validations on NNP

4.3.1 NNP training

The DFT data set for training NNPs consists of pure phases, solid solutions, and their melts. For pure phases of MgO and CaO, the data set first contains rocksalt crystals under volume-conserving uniaxial, hydrostatic, or shear strain, whose ranges are –5% to 5%, –2% to 4%, and –5% to 5%, respectively. For intermediate compositions, we generate 100 random alloys in the rocksalt structure ($Mg_xCa_{1-x}O$) containing 100 atoms in $x = 0.08, 0.2, 0.8, 0.92$. For each composition, the lattice parameter is obtained by relaxing the cell shape and volume. To sample thermal vibrations of solids as well as liquid phases, the crystals of pure phases and random alloys (the most and least stable configurations among the 100 structures) are heated from 300 K to 2000, 4000, 6000, and 8000 K with a duration time of 1 ps at each temperature. Two independent MD simulations are performed in constant pressure (NPT) or constant volume (NVT) ensembles, where temperatures are modulated with the Langevin [107] or Nosé-Hoover [108] thermostats, respectively. We note that both ensembles are complementary in constructing data sets; while the NPT data set includes the thermal expansion of solid and liquid phases, NVT data set contains interactions between atoms at short distances, which helps prevent short-bond failures of NNPs during MD simulations along the thermodynamic integration path. We find that the pure phases and random alloys melt at 8000 and 6000 K, respectively. By including these melting processes, NNP may learn the interface between the solid and liquid phases required for coexistence simulations. Those MD trajectories are sampled with the interval of 40 and 10 fs at 300–4000 K and 6000–8000 K, respectively, and included in the data set after accurate single-shot DFT calculations. The whole data set contains 5,670 structures, equivalent to 552,096 atoms, consistently for both PBE and SCAN as shown in Table 4.1.

We generate single NNP for PBE and SCAN functionals, named as PBE-NNP and SCAN-NNP, respectively, which is used for the whole calculations. 10% of the data

Table 4.1: Data set statistics. The same protocol for constructing data sets is used for both PBE-NNP and SCAN-NNP.

Type	x ($Mg_xCa_{1-x}O$)	Temperature (K)	MD time (ps)	Sampling interval (fs)	Number of structure	Number of atoms
Strained crystal	0, 1	0	-	-	162	1,296
Random alloys	0.08, 0.2, 0.8, 0.92	0	-	-	8	800
Melting pure rocksalt (NVT, NPT)	0, 1	300, 2000, 4000	1	40	300	30,000
		6000, 8000	1	10	800	80,000
Melting random alloy (NVT, NPT)	0.08, 0.2, 0.8, 0.92	300, 2000, 4000	1	40	1,200	120,000
		6000, 8000	1	10	3,200	320,000
Total					5,670	552,096

is randomly selected as a test set to evaluate performance of the NNP. The root mean square error (RMSE) of NNPs on the training and test set is presented in Table 4.2, indicating that the accuracy of NNPs is satisfactory. The parity plots in Fig. 4.1 display correlations of the energy and force components between DFT and NNP for the test sets, showing that both PBE-NNP and SCAN-NNP well reproduce the reference DFT results. The slightly higher energy RMSE of SCAN-NNP (Table 4.2) could be attributed to a wider energy range of the data set as seen in Figs. 4.1(a) and (b). In comparison, the force RMSE between the two NNPs is comparable since the magnitude of the force is similar in both data sets (see Figs. 4.1(c) and (d)).

Given that the final model is subject to the hidden layer architectures or the random numbers that determine initial weights of neural networks, the influence of the network dimension can be partly examined by the four NNPs with varying numbers of hidden nodes that were developed for estimating prediction uncertainties in Fig. 4.2. They have two hidden layers of 30, 60, 100, or 150 nodes and trained on different training sets from the same data set. When we calculate melting points of the pure phases using those NNPs, the deviations between NNPs are less than 20 K (see below). Moreover, the standard deviation of substitutional defect formation energy among those NNPs is only about 1% within SCAN-NNPs.

4.3.2 Test of NNP on pure phases

In Table 4.3, the trained NNPs are further validated by comparing various properties of pure phases. We first compare structural and mechanical properties of rocksalt MgO and CaO at 0 K. It is seen that PBE overestimates the lattice parameters by 0.6–0.8%, while SCAN underestimates by 0.3–0.6%, in better agreements with experiment [109, 110]. The elastic constants are also reproduced more accurately by SCAN than PBE, except for C_{12}. It is seen that each NNP well reproduces corresponding DFT results—lattice parameters within 0.001 Å and elastic constants within 16.7% (largest for off-diagonal component C_{12} in SCAN-NNP).

Table 4.2: The root mean square error (RMSE) for the energy and force on training and test sets. PBE-NNP and SCAN-NNP represent NNPs that are trained with the corresponding functional. In averaging errors in the force, the three-dimensional Euclidean distance is measured between DFT and NNP forces.

	Energy (meV/atom)		Force (eV/Å)	
	Train	Test	Train	Test
PBE-NNP	4.0	4.1	0.24	0.28
SCAN-NNP	5.1	5.5	0.24	0.29

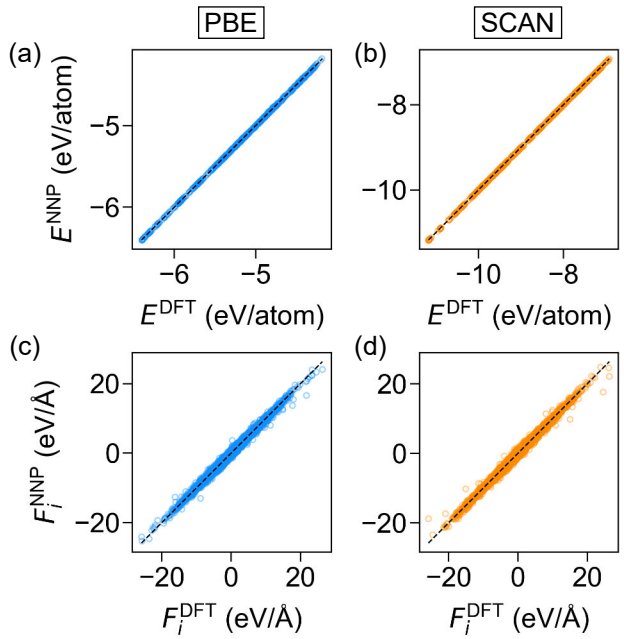

Fig. 4.1: Parity plots between DFT and NNPs, comparing energies (E) ((a) and (b)) and force component ($F_i, i = x, y, z$) in the Cartesian coordinate ((c) and (d)) for test sets. The functional used for the reference data set is shown at the top.

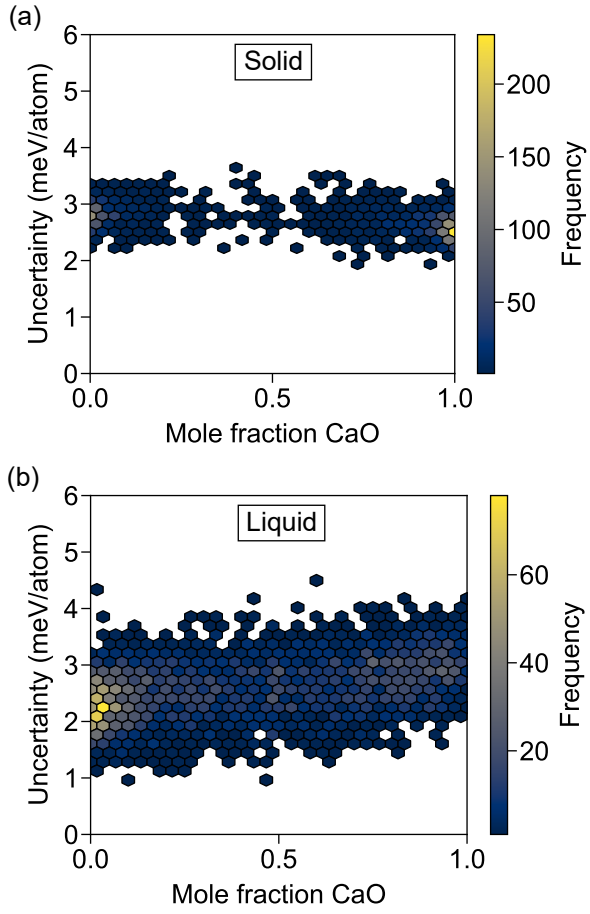

Fig. 4.2: Prediction uncertainty of NNPs during semigrand ensemble simulations of (a) solid and (b) liquid phases. Note that the uncertainty is < 5 meV/atom for all the trajectories spanning concentrations.

Table 4.3: Equilibrium lattice parameter (a_0), bulk modulus (B), and elastic constants (C_{11}, C_{12} and C_{44}) of rocksalt MgO and CaO at 0 K. The properties are calculated after cell relaxations, and elastic constants are calculated by applying strains smaller than 0.5%. Relative errors are presented in the parentheses with respect to the experiments (for DFT) or DFT calculations (for NNP), respectively.

	Property	PBE	PBE-NNP	SCAN	SCAN-NNP	Experiment
MgO	a_0 (Å)	4.246 (0.8%)	4.247 (0.0%)	4.186 (–0.6%)	4.186 (0.0%)	4.213[a]
	B (GPa)	153.3 (–6.9%)	158.6 (3.4%)	174.4 (5.9%)	170.9 (–2.0%)	164.7[b]
	C_{11} (GPa)	273.8 (–10.7%)	281.4 (2.8%)	327.1 (6.6%)	317.6 (–2.9%)	306.7[2]
	C_{12} (GPa)	93.1 (–0.6%)	97.3 (4.5%)	98.0 (4.6%)	97.6 (–0.5%)	93.7[2]
	C_{44} (GPa)	145.2 (–7.9%)	132.4 (–8.8%)	160.8 (2.0%)	146.0 (–9.2%)	157.6[2]
CaO	a_0 (Å)	4.839 (0.6%)	4.840 (0.0%)	4.797 (–0.3%)	4.797 (0.0%)	4.811[1]
	B (GPa)	105.2 (–7.7%)	105.5 (0.3%)	115.8 (1.6%)	118.5 (2.4%)	114.0[1]
	C_{11} (GPa)	203.1 (–9.0%)	203.6 (0.2%)	241.7 (8.2%)	232.3 (–3.9%)	223.3[1]
	C_{12} (GPa)	56.3 (–5.0%)	56.5 (0.3%)	52.8 (–10.9%)	61.7 (16.7%)	59.3[1]
	C_{44} (GPa)	74.8 (–7.7%)	70.7 (–5.4%)	86.0 (6.2%)	76.3 (–11.3%)	81.0[1]

[a]Reference [109].

[b]Reference [110].

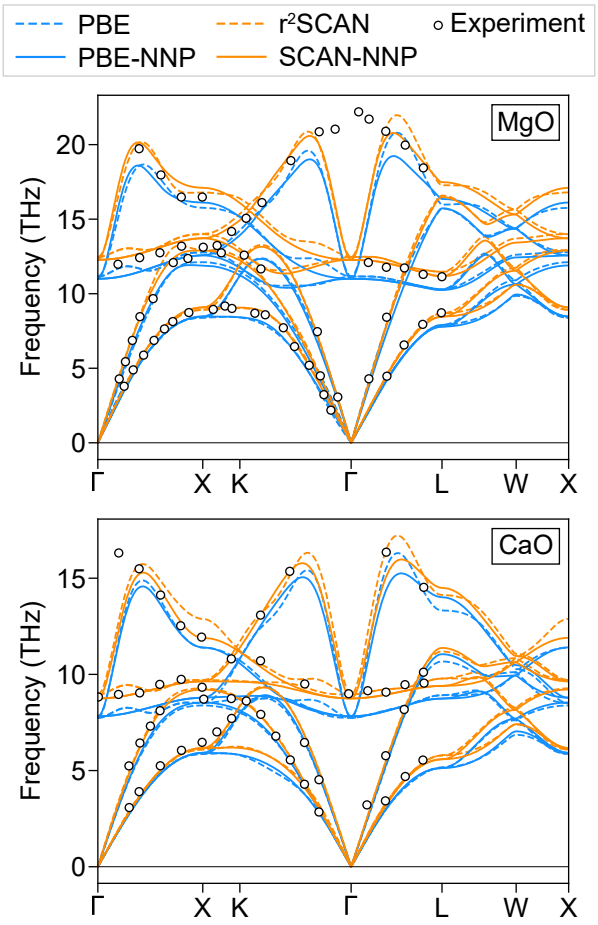

Fig. 4.3: Phonon dispersion along the high-symmetry points of the rocksalt phase of MgO and CaO. We use the r^{2}SCAN functional instead of the original SCAN in this case for better numerical convergence of lattice dynamics [101]. Experimental measurements are adopted from Refs. [112] (MgO) and [113] (CaO).

In Fig. 4.3, we compute phonon dispersions and compare them with experiments. The phonon dispersions are calculated using the `Phonopy` code [56] with the finite displacement method and a 5×5×5 repetition of the primitive cell. In Ref. [101], it was tricky to obtain phonon dispersions with the SCAN functional due to unstable convergences, which is also confirmed in the present work as the phonon dispersions calculated within the SCAN functional exhibit spurious imaginary modes for rocksalt MgO and CaO. Instead, we employ r^{2}SCAN functinoal [111] for phonon calculations, as it exhibits better numerical convergences while maintaining the accuracy of the original SCAN. As shown in Fig. 4.3, the r^{2}SCAN functional accurately reproduces the lattice dynamics of the experiments [112, 113]. On the other hand, PBE calculations underestimate the phonon frequencies. We do not consider the modifications of optical branches due to the long-range Coulomb interactions (LO-TO splitting), resulting in the deviations of optical branches near the Γ point. In Fig. 4.3, NNPs successfully reproduce the phonon dispersions by DFT regardless of the functional type.

To benchmark thermal properties of solids at constant pressures, the linear coefficient of thermal expansion (CTE) and heat capacity (C_{p}) are calculated in Fig. 4.4 within the quasi-harmonic approximation [56]. As can be seen in Fig. 4.4(a), for both pure phases, the predicted CTE in SCAN-NNP compares favorably to the experiments, whereas PBE-NNP overestimates it by about 20-30%. Similarly, Fig. 4.4(b) shows that C_{p} of MgO agrees well between SCAN-NNP and experiment, while PBE-NNP slightly overestimates it. For CaO, C_{p} is accurately predicted by both NNPs, although SCAN-NNP and PBE-NNP perform slightly better at temperatures below and above 350 K, respectively.

We next compare structural properties of the liquid phases, which are obtained by employing 100-atom supercells and NVT ensembles with temperatures of 3100 and 2850 K for MgO and CaO, respectively. The radial and angular distribution functions (RDF and ADF, respectively) are averaged over 40-ps MD simulations, preceded by 5-ps pre-melting at twice the temperature and 10-ps equilibration. The total and atom-

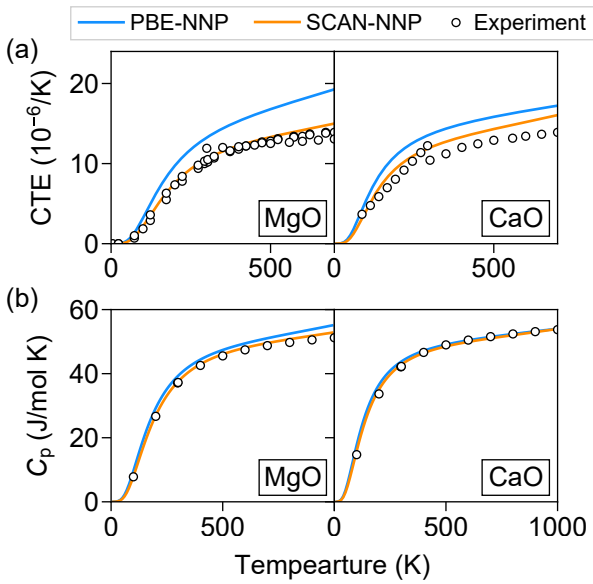

Fig. 4.4: Thermal properties of MgO and CaO calculated by quasi-harmonic approximations: (a) linear coefficient of thermal expansion (CTE) and (b) heat capacity at constant pressure (C_{p}). Experimental values of CTE for MgO and CaO are from Ref. [114–116] and Ref. [116, 117], respectively, while C_{p} is from the thermochemical tables [118].

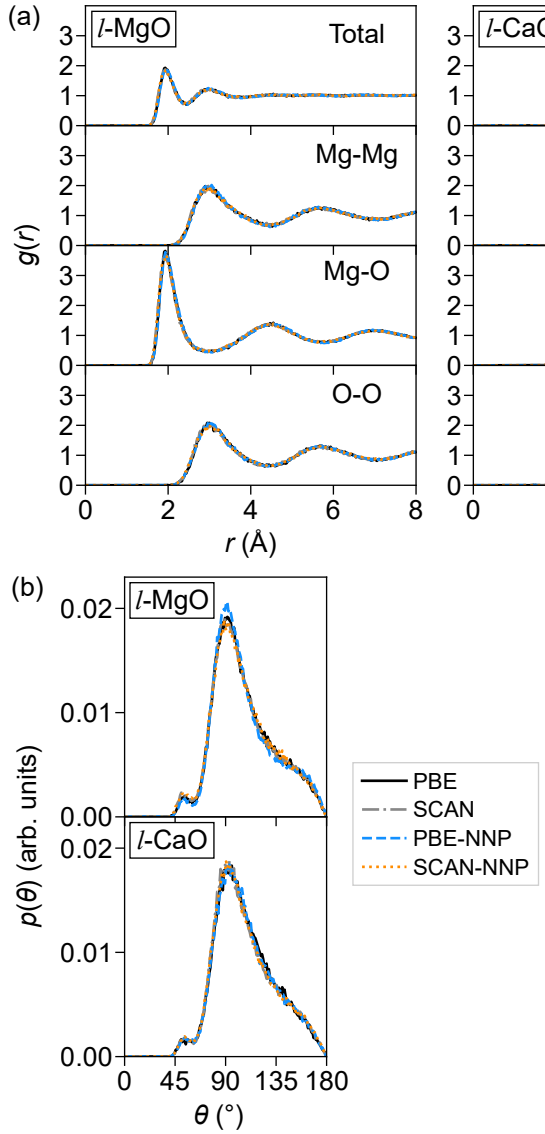

Fig. 4.5: (a) Total and partial radial distribution functions ($g(r)$) and (b) total angular distribution functions ($p(\theta)$) of liquid MgO and CaO.

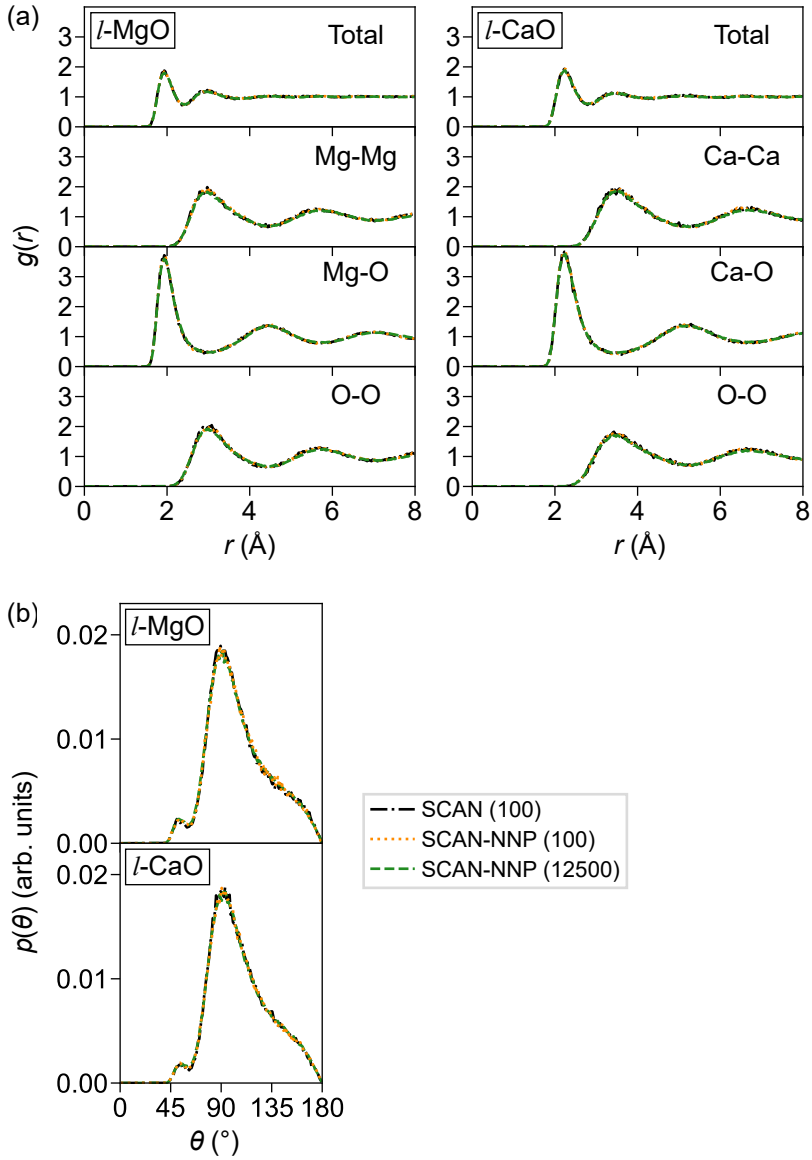

Fig. 4.6: (a) Total and partial radial distribution functions ($g(r)$) and (b) total angular distribution functions ($p(\theta)$) of liquid MgO and CaO in large supercells. The number of atoms within the simulation cells are shown in the parentheses.

resolved RDFs in Fig. 4.5(a) indicate that the first peaks are dominated by heteropolar pairs for both liquid MgO and CaO (l-MgO and l-CaO, respectively). The first peaks lie at 2.0 and 2.2 Å for MgO and CaO respectively, where the difference stems from the larger ionic radius of Ca than that of Mg. The second peaks consist of mostly homopolar pairs, with similar distributions among the pairs. The ADFs are shown in Fig. 4.5(b), and both phases commonly exhibit a major peak at 90° and shoulder peaks around 50° and 150°. Both NNPs well reproduce main features in the RDF and ADF from DFT calculations. In addition, the RDF and ADF are also consistent in 12,500-atom supercells, as shown in Fig. 4.6. It is noticeable that the liquid structures of PBE-NNP and SCAN-NNP are hardly distinguishable despite the significant differences in the solid phase.

4.3.3 Test of NNP on pseudo-binary mixtures

In this subsection, we test the accuracy of NNPs for solids and liquids at intermediate compositions. To this end, we first compare the formation energies of substitutional defects in solids that affect the free energy of mixing at low concentrations. The defect formation energy (D_{f}) is defined as follows:

$$D_{\mathrm{f}} = E_{\mathrm{defect}} - \sum_i N_i E_i, \tag{4.8}$$

where E_{defect} means the total energy of the supercell containing a point defect, and N_i and E_i ($i = \mathrm{MgO}, \mathrm{CaO}$) indicate the number of formula unit in the supercell and the energy of pure phases, respectively. As can be seen from Table 4.4, NNPs reproduce DFT formation energies of the substitutional defects within 3%. Both PBE and SCAN produce a larger D_{f} for $\mathrm{Ca}_{\mathrm{Mg}}$ than for $\mathrm{Mg}_{\mathrm{Ca}}$, which implies a lower solubility of the former. It is also seen that SCAN produces a higher D_{f} than PBE by 0.2 eV, which affects the solubility limit as will be shown later.

Next, we compare the formation energies of ordered structures at intermediate compositions. We consider ten ordered structures [119] by exchanging cations in the

Table 4.4: The formation energy of substitutional defects in eV. $\mathrm{Ca_{Mg}}$ and $\mathrm{Mg_{Ca}}$ mean a single-atom impurity of CaO in MgO and MgO in CaO respectively, where we use 216-atom supercells to evaluate the formation energy of point defects.

Type	PBE	PBE-NNP	SCAN	SCAN-NNP
$\mathrm{Ca_{Mg}}$	1.00	0.98	1.21	1.19
$\mathrm{Mg_{Ca}}$	0.67	0.70	0.86	0.82

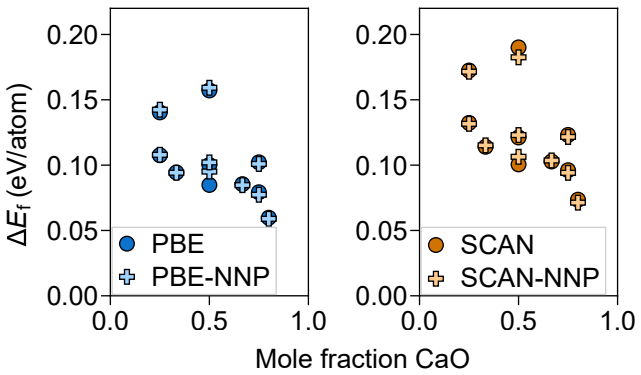

Fig. 4.7: Formation energy (ΔE_{f}) of ten ordered structures evaluated within PBE or SCAN functional and corresponding NNPs.

rocksalt lattice, including $L1_0$, $L1_1$, NbP, Ni_4Mo, $L1_2$, $D0_{22}$, and $MoPt_2$ structures where the latter three structures include both Mg- and Ca-rich stoichiometries. The formation energy per atom (ΔE_f) is defined as follows:

$$\Delta E_\mathrm{f} = \frac{1}{2\sum_i N_i}\left[E_\mathrm{SC} - \sum_i N_i E_i\right], \tag{4.9}$$

where E_SC means the total energy of the ordered structure and other notations are the same as in Eq. 4.8. The ΔE_f's computed by DFT and NNPs are compared in Fig. 4.7, showing that NNPs closely reproduce corresponding DFT results within 10 meV/atom. It is understandable that the errors in ΔE_f are maximum at $Mg_{0.5}Ca_{0.5}O$, as the training set consists of pure phases and mixtures of up to 20% mole fractions. It is seen that none of the ordered phases are energetically favorable with respect to the pure phases, with ΔE_f greater than 50 meV/atom. We also note that the magnitude of ΔE_f is larger in SCAN than PBE, which is consistent with D_f.

As a preliminary test to see behaviors of cations in solid solution before calculating phase diagram, we perform hybrid MC-MD simulations of halite phase with $Mg_{0.5}Ca_{0.5}O$ stoichiometry at 1200 K. We employ NPT ensemble with 1-fs time step, and the initial configuration is given by random solid solutions containing 8,000 atoms and equilibration of 10 ps. Then in the subsequent 200 ps, Mg–Ca cation pairs are allowed to exchange their sites at 0.2% of the cations per time step, according to the Metropolis criterion. These exchanges accelerate the diffusion process of cations during the annealing. As a measure of distribution of cations, we take the average over the number of cation pairs that are within 4 Å, corresponding to the second nearest neighbors in rocksalt lattice. As shown in Fig. 4.8(a), the number of Mg-Mg and Ca-Ca pairs increases over time from 6 corresponding to a random occupation, while the number of Mg-Ca pairs decreases. This indicates that mixing is energetically unfavored, as is consistent with the positive formation energy of substitutional defects (Table 4.4) and ordered structures (Fig. 4.7).

In addition, as seen from the atomic structure in Fig. 4.8(b), the random configuration is divided into MgO- and CaO-rich regions at 200 ps. The large difference

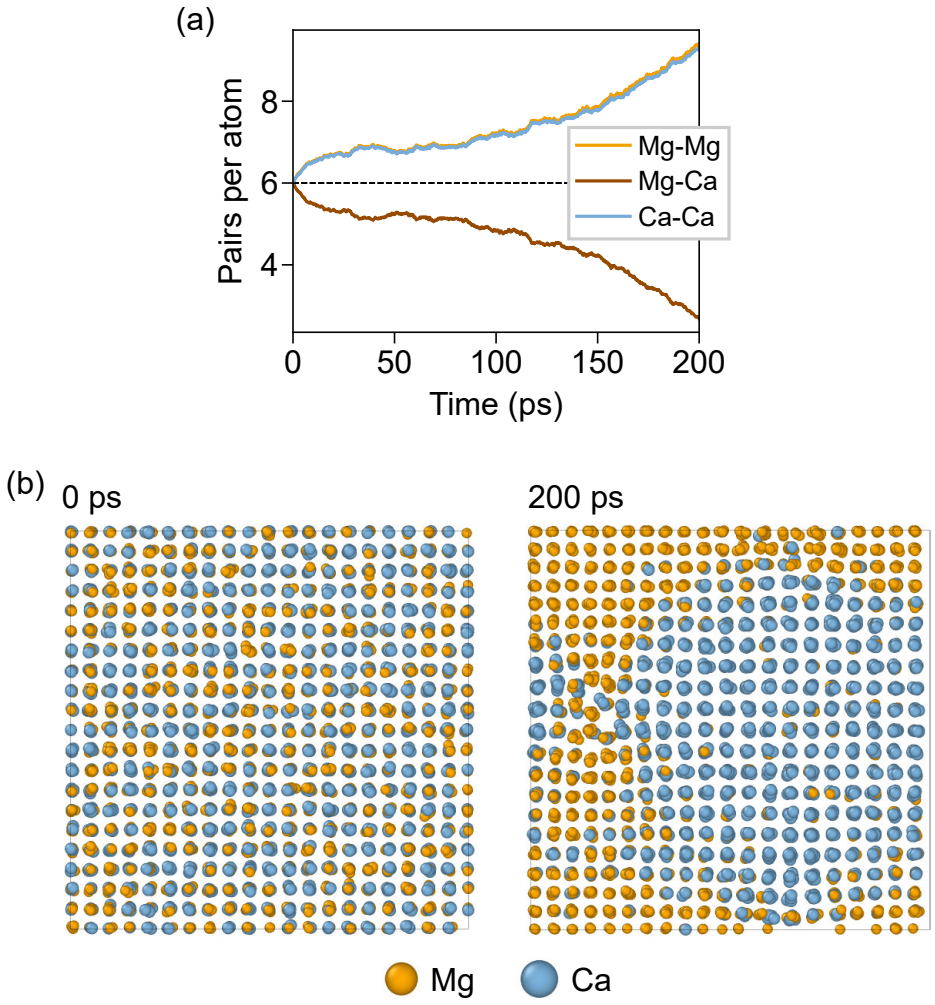

Fig. 4.8: (a) Time evolution of the average number of second nearest-neighbor cation pairs in $Mg_{0.5}Ca_{0.5}O$ simulated by hybrid MC-MD simulations at 1200 K and (b) snapshot at 0 and 200 ps. Atomic structures are visualized without O atoms for clarity.

in lattice parameters between rocksalt MgO and CaO ($\sim$14%) leads to distortion of the cubic lattice by local contraction and expansion at corresponding region. This distortion eventually contribute to the formation of line defects near the boundaries, as seen from the middle-left region at 200 ps, which indicates that the formation of grain boundaries may be energetically favored over misfit deformation. From these aspects, one would expect spinodal decomposition at this temperature and composition, which will be verified in the next section.

4.4 Free energy calculations and phase diagram

4.4.1 Free energy of pure phases

With the accuracy on solid and liquid phases confirmed, the trained NNPs are used in the thermodynamic integration to calculate free energies of the solid and liquid phases. We employ a 10-point Gauss-Legendre quadrature to evaluate the integral in Eq. 4.2 using the lattice parameters obtained from NPT simulations at zero pressure (see Fig. 4.9). For all the phases, each point in the quadruture is evaluated by employing a 1,000-atom supercell and 2-ps equilibration followed by 5-ps sampling for the temporal average. We use the Langevin thermostat [107] with the center of mass fixed to avoid drift of the atoms [64, 120, 121]. To determine convergence, we use the block standard error (BSE) as a measure of uncertainty [122].

Figure 4.10 shows the computed free energies of pure phases, which are fitted to an analytical free energy model as follows:

$$G^{\circ}(T) = a + bT + cT\ln T + dT^2 + e/T, \tag{4.10}$$

where a, b, c, d, and e are fitting parameters. Similar function forms were used in the previous thermodynamic calculations [62] and MD studies [120, 123]. The error of fit is less than 2 meV/atom in both solid and liquid phases, which is on the order of the BSE of each point and sufficient to obtain melting properties. By fitting to the smooth function in Eq. 4.10, the determination of temperature-dependent free energies becomes robust against statistical fluctuations in the numerical integration. We add that the specific function form has negligible effects on the melting properties as long as the free energy data are well fitted into the model.

The resulting free-energy curves of MgO and CaO are shown in Fig. 4.10 as solid lines, and the parameters of Eq. 4.10 are tabulated in Table 4.5. Melting properties obtained from intersections of the free-energy curves are summarized in Table 4.6. The melting point of MgO is calculated as 2787 K by PBE-NNP, which is consistent with

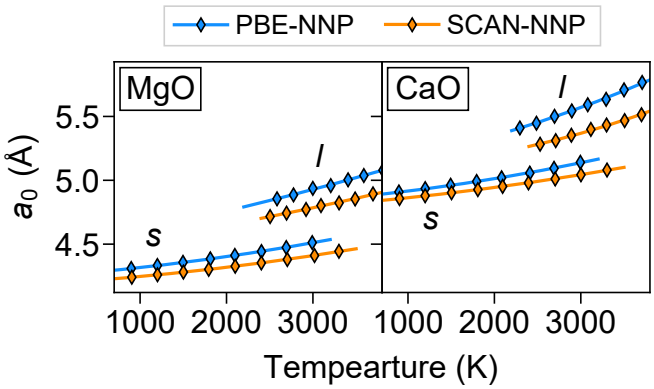

Fig. 4.9: Temperature-dependent lattice parameters of rocksalt (s) or liquid (l) phases of pure MgO and CaO.

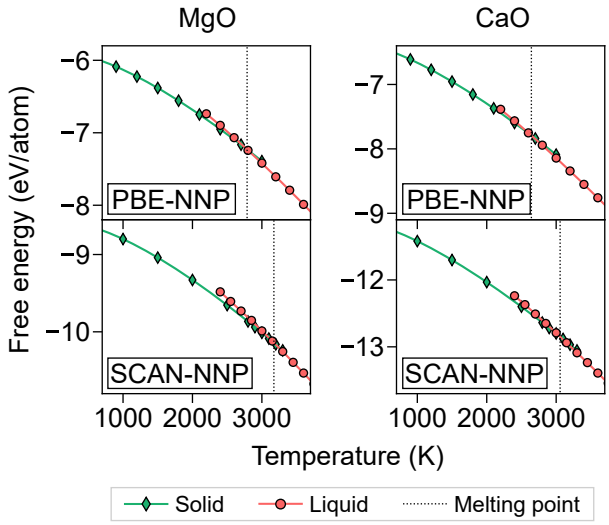

Fig. 4.10: Free energy curves of rocksalt and liquid phases of MgO and CaO. Free energies that are directly calculated from the thermodynamic integration are represented by diamonds (solid) and disks (liquid), and the free energy models are shown in solid lines. Melting points are indicated by vertical dotted lines at the intersection of the free energy curves.

Table 4.5: Parameters of free energy curves for pure phases. a, b, c, d, and e are referred to Eq. 4.10, where G° and T are in units of eV and K, respectively.

Functional	System	a	b	c	d	e
PBE	MgO (s)	-5.9431e+00	1.5145e-03	-2.4410e-04	-1.4229e-08	-1.3176e+00
	MgO (l)	1.2440e+00	-1.7439e-02	1.9615e-03	-2.5464e-07	-3.5113e+03
	CaO (s)	-6.3852e+00	1.3757e-03	-2.3660e-04	-1.6364e-08	-2.0536e+00
	CaO (l)	-4.5441e+00	-1.6308e-03	8.0668e-05	-3.4459e-08	-9.9648e+02
SCAN	MgO (s)	-8.6416e+00	1.5812e-03	-2.5016e-04	-1.1753e-08	2.5882e-01
	MgO (l)	-1.6663e+01	2.4806e-02	-2.9826e-03	2.7552e-07	4.2521e+03
	CaO (s)	-1.1153e+01	1.3307e-03	-2.2835e-04	-1.7090e-08	-3.2114e+00
	CaO (l)	1.8063e+01	-7.9948e-02	9.2978e-03	-1.0596e-06	-1.4408e+04

Table 4.6: Melting point (T_{m}), entropy of fusion (ΔS_{m}), and slope of the melting curve (dT/dP) of MgO and CaO. PBE-GAP and SCAN-GAP represent the Gaussian approximation potential (GAP) trained by the PBE and SCAN data sets, respectively. Approaches refer to thermodynamic integration (TI), coexistence method (Coexist), and interface pinning method with a correction by thermodynamic perturbation theory (IP+TP) [66]. The block standard errors are also provided. Results are from this work unless references are given.

	Property	PBE-NNP	PBE-NNP	SCAN-NNP	SCAN-NNP	PBE[a]	SCAN[1]	PBE-GAP[b]	SCAN-GAP[2]
MgO	T_{m} (K)	2787±30	2786±1.5	3173±33	3181±1.7	2747±59	3032±53	2698±23	3072±25
	ΔS_{m} (k_{B}/atom)	1.61	-	1.58	-	1.63	1.70	1.57	1.50
	dT/dP (K/GPa)	150	-	140	-	155	134	153	140
	Method	TI	Coexist	TI	Coexist	TI	TI	IP+TP	IP+TP
CaO	T_{m} (K)	2640±30	2659±1.5	3057±35	3097±2.0				
	ΔS_{m} (k_{B}/atom)	1.65	-	1.56	-				
	dT/dP (K/GPa)	181	-	156	-				
	Method	TI	Coexist	TI	Coexist				

[a]Reference [103].
[b]Reference [93].

the previous works at the PBE level, 2747 K by DFT calculations [103] and 2698 K by the Gaussian approximation potential (GAP) [93]. However, these values are significantly underestimated compared to the experimental range of 3040–3250 K [62, 103]. In contrast, the SCAN-NNP produces an improved melting point of 3173 K, which is within the experimental range and agrees reasonably with the previous SCAN-DFT calculations (3032 K) or SCAN-GAP (3072 K) [93]. The entropy of fusion and slope of melting curve of MgO are mostly consistent among the same functional. On the other hand, the melting point of CaO is computed to be 2640 K by PBE-NNP, which is far below the experimental data of 2850–3220 K [62]. The SCAN-NNP better predicts the melting point of CaO to be 3057 K, which is within the experimental range.

For a further check, the melting points of the pure phases are recalculated with the coexistence method [65, 124]. In this method, the simulation cell contains solid and liquid phases and the interfaces between them, which is directly equilibrated to identify the transition temperature at which the interface stops moving. We employ a 16,000-atom simulation cell that is a $10\times10\times20$ replication of the conventional unit cell. The initial simulation cell is prepared in NPT ensembles, with the initial guess on melting points calculated from the thermodynamic integration. Half of the simulation cell is melt-quenched to the tentative melting point while the other atoms are frozen. Then the simulation cell is equilibrated within the NPH ensemble for 100 ps, and the temperature is sampled for another 100 ps. When we test the cell size effect with 2,000-atom simulation cells, the melting point shifts only by 6 K. As can be seen in Table 4.6, the melting points calculated by the thermodynamic integration and coexistence methods agree within 40 K.

4.4.2 Phase diagram

To construct the full phase diagram, we compute the free energies in semigrand ensembles at intermediate compositions. The isobaric ensemble is used to allow for the volume to change according to the composition during the MD simulations, and the

cell size is the same as in the thermodynamic integration. The ensemble is equilibrated and sampled during 50,000 steps with the 2-fs time step, and attempts to swap between Mg and Ca atoms are set at 1% of the cations per time step. Single run of the semigrand ensemble simulation at given $\Delta\mu$ and T provides the corresponding equilibrium composition x. After carrying out the semigrand ensemble simulations over a set of $(\Delta\mu, T)$, one can obtain composition-dependent Gibbs free energies following the relation in Eq. 4.6.

In Fig. 4.11(a), results from the semigrand simulation using SCAN-NNP are shown for $\Delta\mu = \mu_{\mathrm{CaO}} - \mu_{\mathrm{MgO}}$. With solid solutions at 2400 K, there exists a $\Delta\mu$ range where the equilibrium composition is not unique due to the dependence on the initial composition. Because of this hysteresis, pure phases of MgO or CaO should be used as initial configurations to scan over end compositions. This is the reason why data points are empty for a range of intermediate compositions at 2400 K (and also 2800 K). The hysteresis weakens with the increasing temperature and almost disappears at 3200 K. For the liquid phase, such hysteresis does not exist at any simulation temperature.

The semigrand simulations are carried out for solid and liquid phases at least five temperatures spanning relevant domains in the phase diagram. (For example, in the case of SCAN-NNP, the simulation temperatures for solids (liquids) are sampled from 1200 (2400) K to 3200 (3300) K with the interval of 400 (100) K.) In order to interpolate free energies over the whole phase diagram and obtain $G(x, T)$ via integration of $\Delta\mu(x, T)$ following Eq. 4.6, we introduce analytical models for the free energy [62, 76] and fit them to the simulation data in Fig. 4.11(a). First, the free energy is written as follows:

$$G(x, T) = G_{\mathrm{pure}}(x, T) + \Delta G_{\mathrm{mix}}(x, T), \tag{4.11}$$

where x is the mole fraction of CaO and $G_{\mathrm{pure}}(x, T)$ means the weighted average of free energies of pure phases:

$$G_{\mathrm{pure}}(x, T) = xG^{\circ}_{\mathrm{CaO}}(T) + (1 - x)G^{\circ}_{\mathrm{MgO}}(T), \tag{4.12}$$

where G°_{MgO} and G°_{CaO} are free energies of the pure phases obtained in the previous subsection. In Eq. 4.11, $\Delta G_{\mathrm{mix}}(x,T)$ means the residual free energy of mixing defined as

$$\begin{aligned}\Delta G_{\mathrm{mix}}(x,T) = k_{\mathrm{B}}T[x\ln x + (1-x)\ln(1-x)] \\ +x(1-x)(A+Bx+Cx^2),\end{aligned} \tag{4.13}$$

where the first term corresponds to the ideal free energy of mixing, and the second term reflects the non-ideality with the temperature-dependent parameters A, B, and C. The chemical potential model is derived from the relation in Eq. 4.6, written as

$$\begin{aligned}\Delta\mu(x,T) = \mu_{\mathrm{CaO}} - \mu_{\mathrm{MgO}} = \frac{\partial G(x,T)}{\partial x} \\ = G^{\circ}_{\mathrm{CaO}}(T) - G^{\circ}_{\mathrm{MgO}}(T) + k_{\mathrm{B}}T\ln\left(\frac{x}{1-x}\right) \\ +A + 2(B-A)x + 3(C-B)x^2 - 4Cx^3.\end{aligned} \tag{4.14}$$

Equation 4.14 is fitted to the simulation data in Fig. 4.11(a), and the optimized models in solid lines are in good agreements with the simulation data. The parameters A, B, and C are assumed to be linear with the temperature as in Ref. [62], and the fitting RMSE of the solid phase is 5.1 and 7.3 meV/atom for PBE-NNP and SCAN-NNP, respectively, and the corresponding RMSEs in the liquid phase are 3.6 and 5.8 meV/atom, respectively.

Figure 4.11(b) shows the fitted ΔG_{mix} in Eq. 4.13 at the selected temperatures, and the parameters are compiled in Table 4.7. At 2400 K, the free energy curve for the solid phase features a miscibility gap resulting from the two local minima at terminal solutions, while no liquid phase is thermodynamically stable throughout the composition. At the elevated temperature of 2800 K, the liquid phase becomes stable over a range of intermediate compositions, and so the eutectic point is expected to lie between 2400 K and 2800 K. Above 3200 K, the liquid phase is always stable over the solid phase as the temperature becomes higher than the melting point of both pure phases. The dotted lines in Fig. 4.11(b) are common tangents of stable phases, and the contacts are indicated by the circles. These contacts represent the phase boundary since

the coexistence of those phases is thermodynamically favored over other compositions and phases.

The full phase diagrams constructed with NNPs are shown in Fig. 4.12 together with experimental data. Based on the fitted analytical free energy models, we calculate the phase boundaries with the 1 K interval between 1200 and 3200 K. It is seen that both PBE-NNP and SCAN-NNP reproduce the characteristics of the MgO-CaO system such as eutectic points and solubility limits. In detail, the eutectic compositions predicted by PBE-NNP and SCAN-NNP are 0.50 and 0.49 for the mole fraction CaO, respectively, which are within the experimental observations of 0.45-0.60 [62] (see red crosses). The eutectic temperature, on the other hand, is 2253 K and 2651 K for PBE-NNP and SCAN-NNP respectively, only the latter being close to the experimental range of 2550-2640 K. The failure of PBE-NNP is consistent with the underestimated melting points of the pure phases. The experimental solid solubility of CaO in MgO (MgO in CaO) at the eutectic temperature is 6% (22%) mole fraction CaO [125], which are closely reproduced by SCAN-NNP within the error bar. The PBE-NNP can also reproduce the solid solubility of CaO in MgO at its own eutectic temperature, but the solubility of MgO in CaO is overestimated by about 10%. The overestimation is related to the smaller formation energy of substitutional defects than with SCAN-NNP (see Sec. 4.3.3), which leads to thermodynamic preference toward mixing. Other experimental data regarding the solvus, solidus, and liquidus are all in good agreements with those by SCAN-NNP.

Figure 4.13 compares the phase diagram by SCAN-NNP and those from other atomistic simulations (see gray lines). Previous theoretical works identified only solid-state phase diagrams of the MgO-CaO system with classical potentials [7, 126] or first-principles calculations [7, 119]. (To note, the effect of lattice vibration is considered only in Ref. [7].) It is seen that none of previous works produced correct solvus lines on both MgO- and CaO-rich sides. On the other hand, the results by CALculation of PHAse Diagrams (CALPHAD) modeling are also presented in Fig. 4.13. While solvus

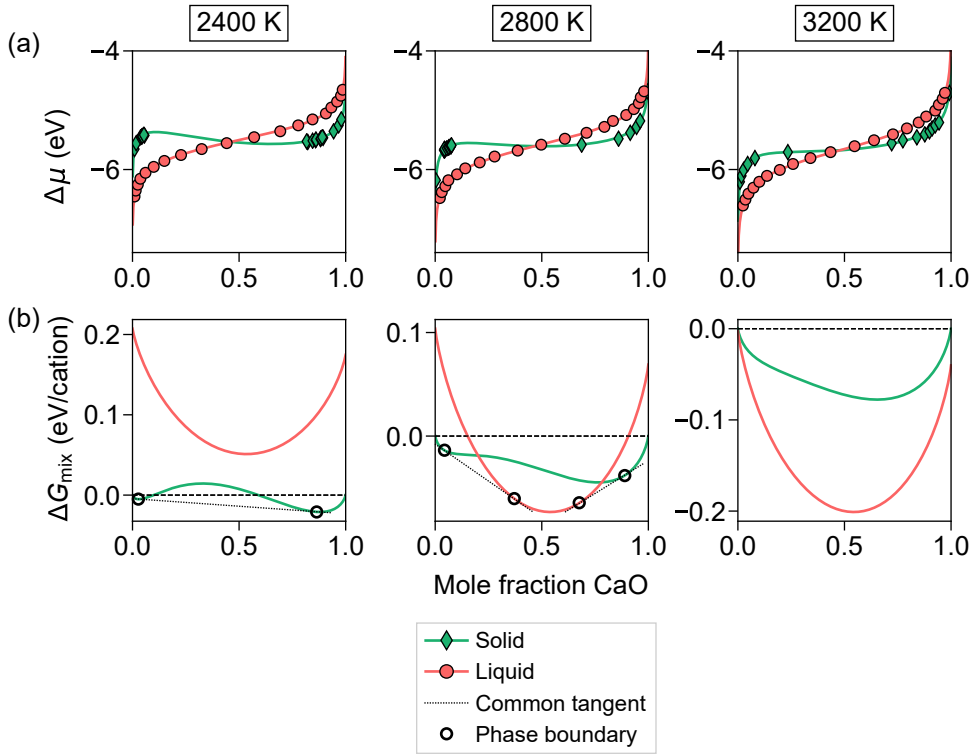

Fig. 4.11: (a) Chemical potential difference ($\Delta\mu = \mu_{\mathrm{CaO}} - \mu_{\mathrm{MgO}}$) and (b) the free energy of mixing (ΔG_{mix}) as a function of composition at selected temperatures, which are calculated with SCAN-NNP. ΔG_{mix} is defined as the difference from the free energy of pure solids. Symbols, solid lines, and dotted lines represent data points obtained from the semigrand ensemble simulations, the fitted free energy models, and the common tangents that determine phase boundary, respectively. Empty circles correspond to the phase boundary at the given temperature.

Table 4.7: Parameters of free energy curves for mixtures. A, B, and C are referred to Eq. 4.13 and are linear to the temperature T in K.

		$A = a_0 + a_1 T$		$B = b_0 + b_1 T$		$C = c_0 + c_1 T$	
Functional	System	a_0	a_1	b_0	b_1	c_0	c_1
PBE	Solid	1.0005e+00	-1.6394e-04	-4.9655e-01	1.1836e-05	1.5641e-01	2.8054e-05
	Liquid	-1.0475e-01	2.1732e-05	-3.0000e-02	1.8798e-05	5.3465e-02	-2.5815e-05
SCAN	Solid	1.2083e+00	-1.7262e-04	-4.3601e-01	-1.3999e-05	7.0239e-03	7.1528e-05
	Liquid	-1.3369e-01	6.0102e-05	3.5721e-02	-1.3233e-05	1.1050e-01	-4.0644e-05

lines are consistent with the SCAN-NNP results, eutectic point, solidus, and liquidus are at variance with each other, even among the CALPHAD data. This is because while solvus lines are validated through a number of experiments, the data for solidus and liquidus lines are sparse and scattered [62]. The mismatch of the phase boundaries from CALPHAD models is understandable because each model is fitted to different sets of data points.

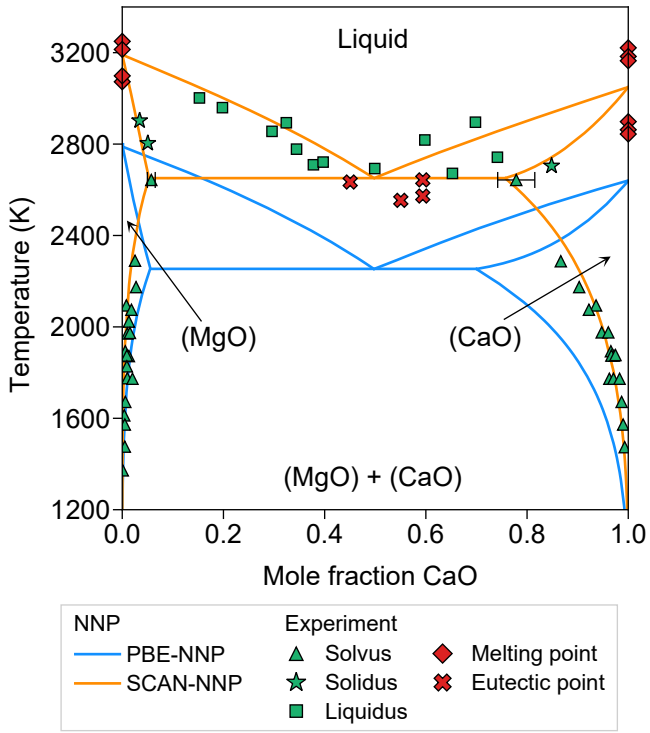

Fig. 4.12: Phase diagrams of MgO-CaO calculated with NNPs, compared to experiments. Experimental solvus, solidus, and liquidus data are from Ref. [62] and the references therein. [17]

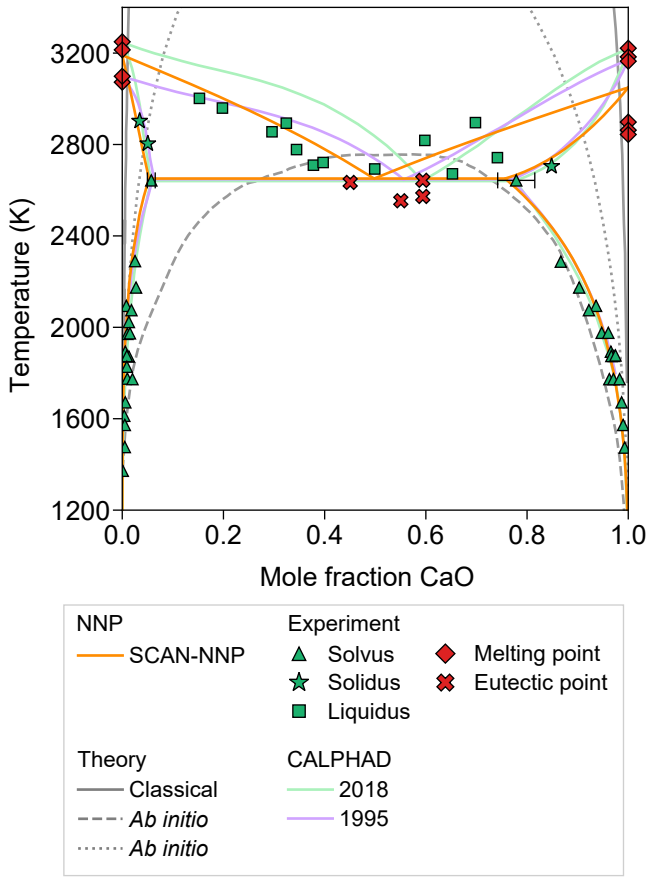

Fig. 4.13: Phase diagrams of MgO-CaO calculated with SCAN-NNP, compared to experiments and other theoretical works or CALPHAD modelings. Theoretical solid-state phase diagrams that are calculated from classical potential (Ref. [7, 126]), first-principles calculations with vibrational effects (Ref. [7]), or tight-binding calculations (Ref. [119]) are displayed in gray lines. The CALPHAD models are adopted from Ref. [62] and Ref. [127]. [17]

4.5 Summary

We remark on the computational efficiency for constructing the phase diagram. The whole procedure, including the data set generation, NNP training, and free energy calculations with MD simulations, took about ten days of computing time on 400 cores of Intel® Xeon® Gold 6148 CPU running at 2.4 GHz. In detail, about five days were spent on generating data sets and training NNPs, and another five days on free energy calculations using NNPs and 1,000-atom cells. If identical free-energy calculations were carried out by purely DFT approaches, it would take several decades with the same computational resource, even assuming that the free energy calculations are done on smaller 200-atom simulation cells. This is mainly because the hybrid MC-MD simulations require a large amount of computing resources due to several million time steps.

In summary, we developed NNPs for the MgO-CaO pseudo-binary system and demonstrated construction of the full phase diagram. The accuracy of NNPs trained over PBE or SCAN data is confirmed by validation over diverse properties. Notably, SCAN-NNP outperformed PBE-NNP in most cases when compared with experiments. The full phase diagrams are determined from the free energy calculations employing thermodynamic integration and semigrand ensemble methods. Notably, SCAN-NNP produced a phase diagram that closely follows experimental measurements on liquidus, solidus, and solvus lines, including the eutectic point and solid solubility limits. In conclusion, we believe that this work will pave the way to the *ab initio* CALPHAD approach with high prediction accuracies.

Chapter 5

From chemical composition to phase diagram: a case study for HfO_2

5.1 Introduction

While Chapter 4 demonstrated that the phase diagram for the pseudo-binary system is constructed accurately compared to experiments, there was an assumption that the phase information is known *a priori*. In other words, the free energy is calculated only for rocksalt and liquid phases in MgO–CaO system since these are experimentally known to be stable at atmospheric pressure. However, given that a large fraction of the chemical space of materials remains unknown [128], it seems necessary to generalize this MLP-based approach to the phase diagram to unexplored chemical spaces.

One of the possible route to achieve this goal is to use theoretical methods such as crystal structure prediction (CSP) [129] to detect stable phases starting from a given chemical element and composition. A number of CSP algorithms have been developed and extensively tested to find the most stable as well as metastable phases for a wide range of systems [14, 130]. The candidate structures are generated based on, for example, informatics, random approaches, and genetic algorithms, and their stability is mostly measured on 0 K energies and lattice dynamics calculated within density-

functional theory (DFT). Whereas it could be valid at low temperatures, prediction of phase stabilization or transition at high temperatures requires another methodologies such as MD simulations and free energy calculations.

In the meanwhile, HfO_2 if of technological importance in electronic applications such as high-k dielectrics, related to its phase transition at finite temperatures [131]. From the room temperature, HfO_2 undergoes two phase transitions: from monoclinic to tetragonal and cubic phases, with space group of $P2_1/c$, $P4_2/nmc$, and $Fm\bar{3}m$, at $\sim$2000 and $\sim$2800 K [131], respectively, before melting at $\sim$3100 K [132]. Furthermore, formation of ferroelectric phase in thin film is known [133], and theoretical investigations suggest a possible polymorph with space group of $Pca2_1$, adding to the difficulty of predicting phase transitions.

With these motivations, this Chapter investigates phase transition of HfO_2 without any prior phase information using a combination of CSP algorithms and NNP. Two different approximations in exchange-correlation energy, PBE and SCAN functional, are also compared with the experiments to test their predictive power. Thermodynamically stable phases and transition among them are investigated based on MD simulations.

5.2 NNP training from chemical composition

5.2.1 Crystal structure prediction

For phase search of HfO_2, we employ CSP algorithm as implemented in SPINNER code [14, 102], which exploits NNPs as a surrogate model of direct DFT calculations. We employ SCAN functional [19] for accurate description of energy of crystal structures, as will be discussed below. Following the standard procedure of this code [102], we start from training of primitive NNPs using *ab initio* melt-quench-anneal simulations to sample local environments at the given chemical composition. After finding candidate crystal structures, they are fully relaxed using DFT calculations to find true local minima. As shown in Fig. 5.1, the primitive NNP has erroneous potential energy surfaces and is not satisfactory to find ground states. To improve accuracy for ordered structures, these NNPs are iteratively trained on the candidates of CSP output until converged. At the final iteration, the NNP energies become accurate for a set of structures, especially at low energies.

Then the crystal candidates are searched for 3,000 generations with the 100 meV/atom energy window. The final candidates are fully relaxed by DFT until a force criteria of 10^{-3} eV/Å and deduplicated with pRDF indicators [102] and the space group. We note that due to the small differences between the structures, high resolution is required to distinguish them: for example, pRDF indicator with threshold of 10^{-5} or space group tolerance of 0.03 Å. As a result, 22 candidates are obtained in total, and their energy and volumes are plotted in Fig. 5.2(a), and detailed information is given in Table 5.1. We note that all three atmospheric pressure phases can be found with this NNP-based CSP algorithm (red circles). In addition, the ferroelectric phase ($Pca2_1$) is also found (a green circle), which is relevant to a large permittivity in thin film [134]. The others include 1 high-pressure phase and 17 theoretical phases (blue circles).

On the other hand, as can be seen in Fig. 5.2(b), results based on PBE functional show that another theoretical phase with the energy almost the same to the ground

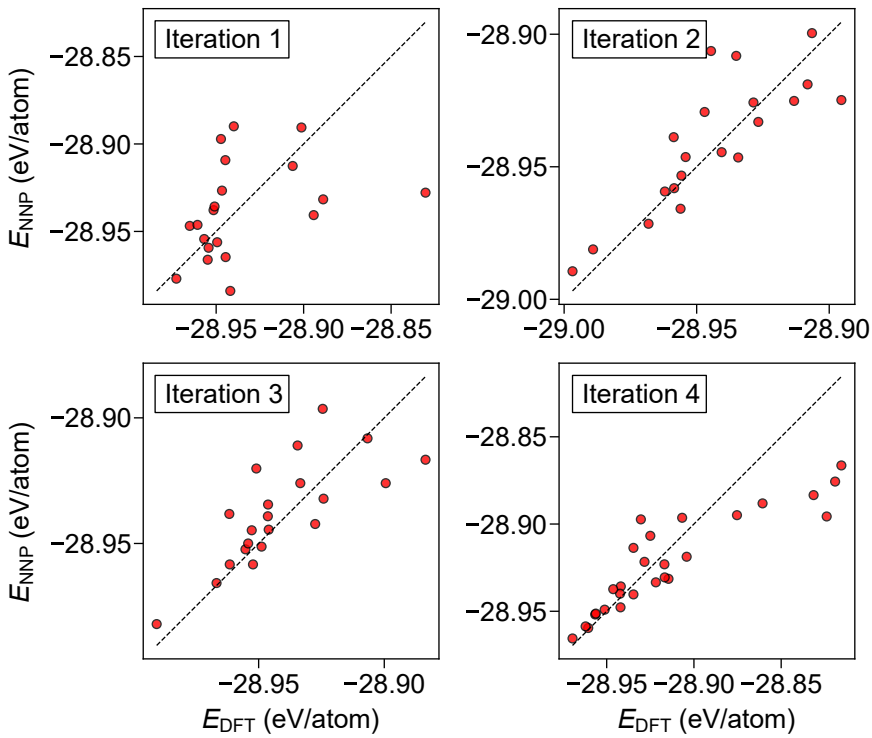

Fig. 5.1: Comparison for structural energy between DFT and NNP during the iterative training. The NNP is trained on total 4 iterations, and the structures obtained from the CSP algorithm are fully relaxed within DFT.

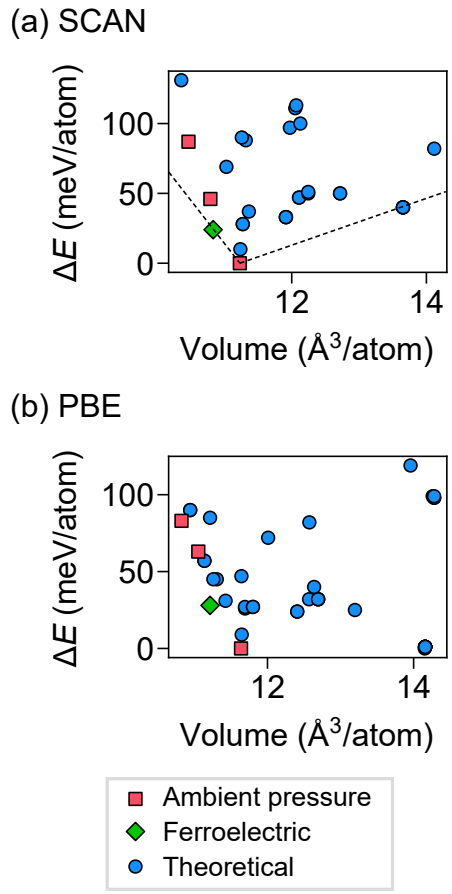

Fig. 5.2: Energy and volume of the final candidates after full relaxation by DFT, using (a) SCAN-NNP and (b) PBE-NNP. Energies are referenced to the ground state, and dashed lines are guide to the eyes.

Table 5.1: CSP results: 22 polymorphs of HfO_2 with space group, energy, and volume. The energy is referenced to the lowest-energy phase. Atmospheric pressure and ferroelectric phases are abbreviated with the notations, and experimentally observed phases are indicated by descriptions in the last column.

No.	Space group	Energy (meV/atom)	Volume (Å^3/atom)	Notation	Expt.
1	$P2_1/c$ (14)	0	11.23	m	Ground state
2	Pbca (61)	10	11.24		High pressure
3	$Pca2_1$ (29)	24	10.83	o	Ferroelectric
4	$P2_1/m$ (11)	28	11.27		
5	Pbcn (60)	33	11.92		
6	Pnma (62)	37	11.36		
7	$I4_1/amd$ (141)	40	13.65		
8	$P4_32_12$ (96)	46	10.79		
9	$P4_2/nmc$ (137)	46	10.79	f	Ambient pressure
10	$P2_1/c$ (14)	47	12.11		
11	Pbca (61)	50	12.72		
12	$P4_2/mnm$ (136)	50	12.25		
13	$P2_1/c$ (14)	69	11.03		
14	C2/m (12)	82	14.12		
15	$Fm\bar{3}m$ (225)	87	10.47	c	Ambient pressure
16	P1 (1)	88	11.32		
17	C2/c (15)	90	11.26		
18	$P\bar{3}$ (147)	97	11.97		
19	$P2_12_12$ (18)	100	12.13		
20	C2/m (12)	111	12.05		
21	Pbcn (60)	113	12.07		
22	Pbcn (60)	131	10.36		

state, whose space group is $I4_1/amd$ and volume 21% larger than the ground state. This could be attributed to the underbinding of the PBE functinoal. This phase has an energy 40 meV/atom higher than the ground state in SCAN, so we do further investigations within the SCAN functional that gives correct energetic order.

5.2.2 Retraining and validations

The NNPs obtained within Sec. 5.2.1 is tested for equations of states and phonon dispersion, but its accuracy is dissatisfactory when compared to the DFT. Therefore, we construct an accurate data set based on the CSP results with two approaches. First, all the candidates are included in the data set with uniaxial, biaxial, hydrostatic, and shear strains. Then, 5 lowest-energy structures (see Table 5.1) are chosen to sample finite-temperature behaviors with NVT- and NPT-AIMD simulations. (Condition of MD simulations are the same to the method in Sec. 4.3.1.) NNPs are retrained on those data set, which have two hidden layers with 60 hidden node each, and the radial and angular cutoff distance is set to be 7 and 5 Å, respectively.

As shown in Fig. 5.3, NNPs can accurately predict the volume and energy of a wide range of polymorphs as well as their strain dependency. Furthermore, energetic order of these structures are also well reproduced, which only differs in meV order. In Fig. 5.4, phonon dispersion is calculated for three polymorphs, including ground state ($P2_1/c$), high-pressure phase (Pbca), and ferroeletric phase ($Pca2_1$). They are all dynamically stable at 0 K, and NNPs well reproduce lattice vibrations compared to the DFT calculations, except for deviations at high-frequency optical modes. The other two atmospheric-pressure phases are not dynamically stable at 0 K, confirmed by imaginary modes.

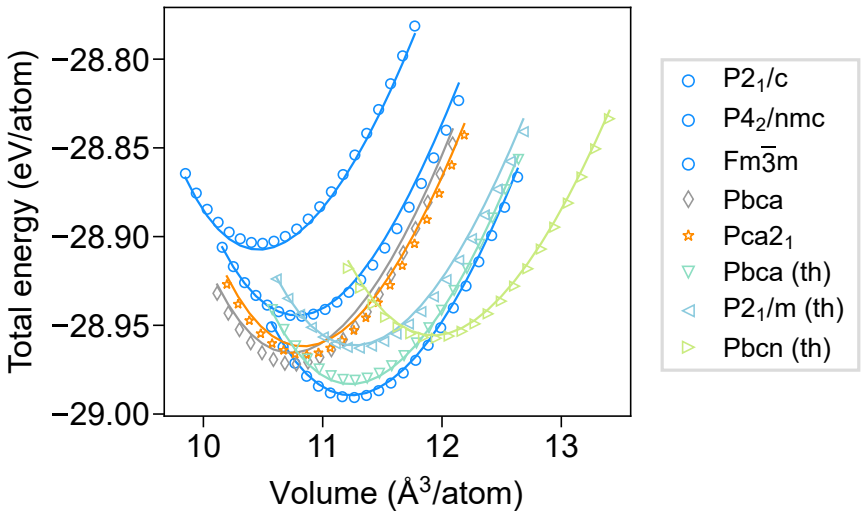

Fig. 5.3: Equations of states of HfO_2 for 8 polymorphs including atmospheric-pressure (circles), ferroeletric (a star), high-pressure (a diamond), and theoretical (triangles) phases. Markers and solid lines correspond to the DFT and NNP, respectively.

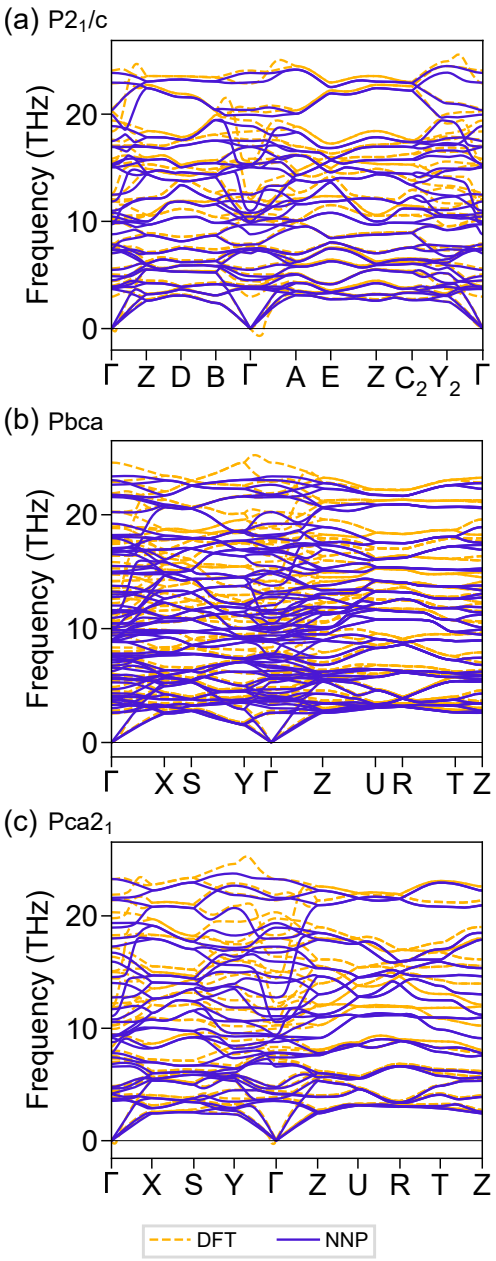

Fig. 5.4: Phonon dispersion of HfO_2 for 3 polymorphs including (a) ground state ($P2_1/c$), (b) high-pressure phase (Pbca), and (c) ferroeletric phase ($Pca2_1$). DFT phonon calculations are done within r^{2}SCAN functional [101, 111].

5.3 Prediction of phase transition

5.3.1 MD simulations

As a next step, we carry out MD simulations with the retrained NNP to detect thermodynamically favored phases at 0 bar. NPT ensemble is employed to address change of the cell shape. Phase detection is based on the time average of lattice parameters and atomic position over at least 50 ps. We employ supercells with side lengths being $\sim$25 Å, which correspond to 5×5×5 replication of the HfO_2 ground state. We notice the cell-size dependence of the MD simulation results; when using smaller supercells containing 96 or 324 atoms, phase transition is not clearly visible due to the large fluctuations in lattice parameters. Therefore, we select a larger simulation cell containing 1,500 atoms, which is beyond the scope of DFT calculations. The cell size dependence of MD simulations on phase transition is also noted in Ref. [135].

Upon the heating of ground state $P2_1/c$ (m-) phase from 300 K, HfO_2 evolves into $P4_2/nmc$ (t-) and $Fm\bar{3}m$ (c-) phase at $\sim$2500 and $\sim$2600 K, respectively. Inversely, when cooling the c-phase from 3000 K, phase transition to t- and m-phases is observed at $\sim$2600 and $\sim$1200 K, respectively, indicating that these phase transitions are reversible. On heating or cooling, m- to t-phase transition temperature shows a large hysteresis, while t- to c-phase transition occurs with little hysteresis. This can be attributed to the phase change barrier stemming from large mismatch of the cell shape and volume between m- to t-phases [136].

To further investigate the thermal stability of the phases from crystal structure predictions, we further perform MD simulations for 5 more phases exhibiting either low energy at 0 K or high symmetries. Selected polymorphs have space group of Pbca, $Pca2_1$, $P2_1/m$, $I4_1/amd$, and $P4_2/mnm$, corresponding to the 2nd, 3rd, 4th, 7th, and 12th rows in Table 5.1, respectively. Among them, $Pca2_1$ phase is known as ferroelectric phase [131]. Upon heating from 500 K to 2500 K, Pbca, $I4_1/amd$, and $P4_2/mnm$ phases maintain the crystal structure, while $Pca2_1$ and $P2_1/m$ phases are transformed into

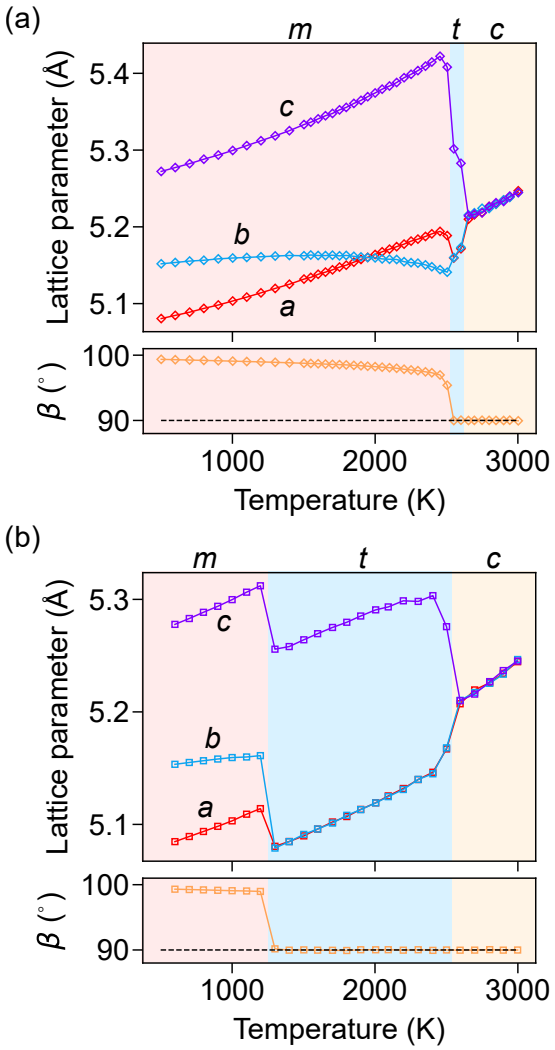

Fig. 5.5: Evolution of lattice parameter (a, b, and c) and angle (β) upon (a) heating and (b) cooling. The markers are simulation data, and the lines are guides to the eye. Phase information at given temperatures is marked by shades.

another phase at 1300 K.

5.3.2 Phase transition temperature

To determine the transition temperature between the phases that appear from MD simulations, we first calculate the free energy of 7 phases with TI method (see Section 4.2.2). Einstein crystal is selected as the reference system to deal with these solid phases, and the free energy data are fitted to Eq. 4.10 to find the intersections. As can be seen from Fig. 5.6, free energy of m-phase is the lowest at low temperatures, and the phase transition to $I4_1/amd$ and t-phase is observed at 1938$\pm$118 and 2456$\pm$96 K, respectively. (The intersection of m- and t-phase is at 2304$\pm$66 K.) The other phases including ferroelectic o-phase is unstable over the whole temperature range. Parameters of free energy curves (Eq. 4.10) are given in Table 5.2.

In the meanwhile, transition to c-phase and liquid are treated with different approaches other than TI method. This is due to the vigorous diffusion of O atoms at elevated temperatures while Hf atoms maintain local vibrations around their ideal position, making it tricky to apply a direct TI path from Einstein crystal to real system. These behaviors would be in line with the small oxygen diffusion barrier in HfO_2 [137], which is comparable to the thermal energy $k_{\mathrm{B}}T$ at the temperatures where c-phase is stable. One would have to seek another integration path that considers self diffusion.

The transition from t- to c-phase has second-order character as seen from continuous changes in lattice parameters at 2450–2600 K without hysteresis (Fig. 5.5). Thus we narrow down the transition temperature by additional MD simulations with 20 K interval, resulting in the t- to c-phase transition temperature of 2550$\pm$10 K. Then the melting point is determined from coexistence simulations between c-phase and liquid (see the last paragraph of Section 4.4.1). We use 5,184-atom simulation cell and NPH ensemble to average the coexistence temperature over 0.6 ns after equilibration of 0.4 ns. This simulation results in the melting point of HfO_2 to be 2745$\pm$6 K.

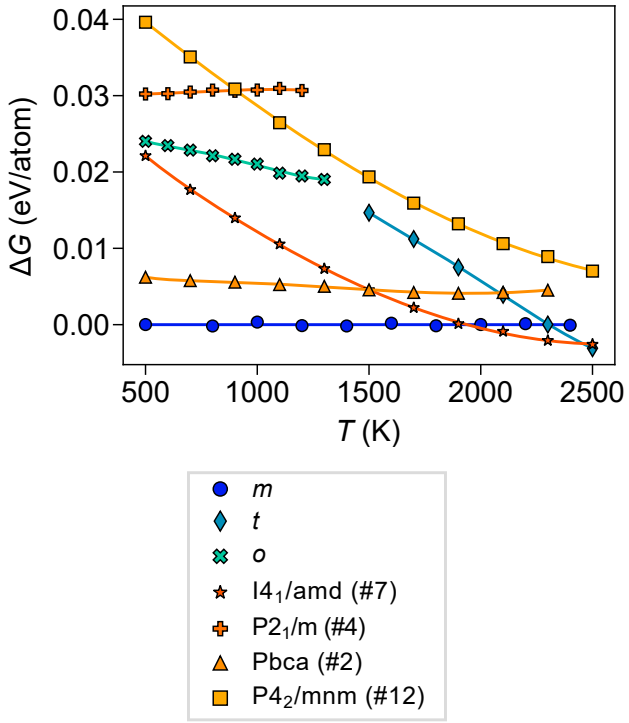

Fig. 5.6: Free energy of HfO_2 polymorphs. The markers indicate free energies calculated from the thermodynamic integration method, and the lines are fitted models. Free energies are referenced to the free energy model of m-phase. Phase notations or the numbering is referred to Table 5.1.

Table 5.2: Parameters of free energy curves for HfO_2 polymorphs. $T_{\min}$ and $T_{\max}$ means the minimum and maximum temperatures at which the free energy is calculated for a given phase, respectively, so that the free energy curves are only valid within those temperature ranges. a, b, c, d, and e are referred to Eq. 4.10, where G° and T are in units of eV and K, respectively.

Phase	$T_{\min}$ (K)	$T_{\max}$ (K)	a	b	c	d	e
m	500	2400	-2.8984e+01	1.5077e-03	-2.4853e-04	-1.1980e-08	-7.3449e-01
t	1500	2500	-3.0718e+01	9.2334e-03	-1.2136e-03	1.6045e-07	5.3674e+02
o	500	1300	-2.9123e+01	3.0345e-03	-4.6194e-04	7.4945e-08	2.0021e+01
$I4_1/amd$ (#7)	500	2500	-2.8968e+01	1.6143e-03	-2.6638e-04	-1.8781e-09	2.2488e+00
$P2_1/m$ (#4)	500	1200	-2.8937e+01	1.3013e-03	-2.1822e-04	-2.9123e-08	-2.1674e+00
Pbca (#2)	500	2300	-2.9018e+01	1.8115e-03	-2.8950e-04	6.4637e-10	5.7039e+00
$P4_2/mnm$ (#12)	500	2500	-2.8940e+01	1.5615e-03	-2.5978e-04	-4.2501e-09	1.4269e-01

The sequence of phase transitions predicted by NNP is similar to the experiment (m, t, c, and liquid phase). It is also consistent that the ferroelectric o-phase is metastable over the whole temperature range. However, the phase transition temperature differs between the NNP (2304, 2550, and 2745 K) and experiments (2000, 2800, and 3100 K) [131, 132], and the stabilization of $I4_1$/amd phase at 1938–2456 K is another difference from the experiment.

These can be attributed to the training set, since MD trajectories of t-, c-, and $I4_1$/amd phases are not explicitly included in the training set. Adding missing structures in the database would help to mitigate these issues, since the accuracy MLP can be improved by complementing the training set. The error can be also explained by the small entropy changes associated with the phase transition of HfO_2, the small angle between two free energy curves at their intersection. Taking transition from m- to t-phase as an example, the entropy change is as small as 0.2 k_{B}, in which the free energy error of 5 meV/atom would be exaggerated to be 284 K error in temperature. Therefore, considering that the training RMSE of NNP on the low-temperature data is $\sim$5 meV/atom, errors for the transition temperature of up to 350 K can be understood by the small entropy changes. More precise models will be required to obtain more accurate phase transition temperatures.

5.4 Summary

To summarize, phase transition of HfO_2 is predicted by NNPs without phase information, as a test for construction of the phase diagram toward unexplored chemical spaces. Crystal structure prediction reproduces all the atmospheric pressure phases as well as the ferroelectric phase. The phase transition from the ground state m-phase to t- and c-phases and liquids are predicted by NNP-MD simulations, as consistent with the experiments. Errors in the transition temperature or in the stabilization of $I4_1$/amd phase would be resolved when using more diverse data set. We believe that this purely theoretical construction of phase transition for HfO_2 will guide future directions toward phase diagram calculations for experimentally unknown systems.

Using the above-mentioned methods, the phase diagram of an arbitrary binary system can be constructed in the following order: first, candidate phases are found through CSP algorithm in diverse composition including pure and intermetallic compounds. Then, NNPs are trained on these candidates and short AIMD simulations, and temperature- and composition-dependent free energies are calculated by NNP-MD simulations. During this procedure, the data set can be augmented based on the candidate phases or uncertainty predictions whenever the accuracy of the model is unsatisfactory. Finally, the phase diagram is determined from the free energy curves by common tangent construction.

Chapter 6

Conclusion

6.1 Summary of results

I first demonstrated a transferable approach for calculating lattice thermal conductivity at *ab initio* accuracy using NNPs. Data set based on *ab initio* MD data set outperforms random displacement or superposition of phonon modes in accuracy. This is mainly because while lattice dynamics are well reproduced by all three methods, anharmonicity such as scattering rates are only consistent when using AIMD data set. When applying this approach for 25 materials that have diverse symmetries and thermal conductivity, I obtain RMSRE of 18.6% with 2-10 fold computational acceleration. Effect of the size of data set is tested, and reducing the data set to 50 structures results in RMRSE of 31% and up to 50-fold speed-up. While the relative errors are within the factor of two, low-symmetry materials tend to have larger errors than high-symmetry ones. Nevertheless, it is still surprising that this approach is applicable for a wide range of materials with uniform computational cost, making it more beneficial for low-symmetry crystals.

I then demonstrated the construction of full phase diagram for MgO–CaO eutectic system. Two different exchange–correlation functional is employed for generating data set, and the NNP trained on each functional well reproduces the corresponding DFT calculations over structural, mechanical, dynamical, and energetical properties.

Melting properties and phase diagram are successfully obtained through free energy calculations based on NNP-MD simulations, including thermodynamic integration and semigrand ensemble methods. While both PBE-NNP and SCAN-NNP reproduce the eutectic nature of the MgO–CaO phase diagram, the phase boundaries predicted by SCAN-NNP closely follow the experimental measurements. These can be related to the comparative results on the enthalpy of formation and lattice dynamics within SCAN functional.

The above demonstration utilizes prior knowledge of the phase information, thus ruling out the possible stabilization of phases other than rocksalt and liquid. To expand phase diagram calculations to the unknown phase space, I calculate the phase transition of HfO_2 without prior knowledge about polymorphism. By employing the CSP algorithm, I can find 22 candidate structures including all three atmospheric-pressure phases. After training NNPs with AIMD or polymorph data, NNP-MD simulations and free energy calculations find the stable phases and transition temperatures. These result is noteworthy in that the phases and their transitions are obtained with only the chemical composition, without any experimental inputs.

6.2 Original contribution to knowledge

This dissertation presents original contribution to knowledge in two ways; first, a computationally efficient and transferable procedure to compute κ_l in near-DFT accuracy is proposed, by showing that NNPs trained on short AIMD trajectories can reproduce κ_l of a wide range of crystal symmetries. It can be said that another option is added to the theoretical methods for calculating κ_l by extending the MLP-based approach toward complex crystal structures, which has been rarely attempted.

Second, *ab initio* construction of MgO–CaO phase diagram is demonstrated using NNPs without experimental parameters, where the eutectic point and phase boundaries closely follow the experimental measurements when trained on SCAN functional. These tasks have been regarded impractical in fully DFT approaches due to the computational cost, and most of the MLP-based works have focused on single-component systems. Furthermore, it is shown that phase diagram calculations may not require phase information, by showing that phase transition of HfO_2 up to melting point can be predicted when employing crystal structure prediction algorithm.

The primary focus of computational research based on DFT has been using experimental information such as crystal structures to predict their properties. I would expect to construct a virtual laboratory that explores materials space from the chemical composition to the formation of phases and materials properties.

Bibliography

[1] J. J. de Pablo, N. E. Jackson, M. A. Webb, L.-Q. Chen, J. E. Moore, D. Morgan, R. Jacobs, T. Pollock, D. G. Schlom, E. S. Toberer, et al., npj Comput. Mater. **5**, 1 (2019).

[2] A. Jain, S. P. Ong, G. Hautier, W. Chen, W. D. Richards, S. Dacek, S. Cholia, D. Gunter, D. Skinner, G. Ceder, et al., APL Mater. **1**, 011002 (2013).

[3] S. K. Das, Y.-B. Kang, T. Ha, and I.-H. Jung, Acta Mater. **71**, 164 (2014).

[4] H. Jang, J. D. Wood, C. R. Ryder, M. C. Hersam, and D. G. Cahill, Adv. Mater. **27**, 8017 (2015).

[5] D. Lee, K. Lee, D. Yoo, W. Jeong, and S. Han, Comput. Mater. Sci. **181**, 109725 (2020).

[6] B. Mortazavi, E. V. Podryabinkin, S. Roche, T. Rabczuk, X. Zhuang, and A. V. Shapeev, Mater. Horiz. **7**, 2359 (2020).

[7] P. D. Tepesch, A. F. Kohan, G. D. Garbulsky, G. Ceder, C. Coley, H. T. Stokes, L. L. Boyer, M. J. Mehl, B. P. Burton, K. Cho, et al., J. Am. Ceram. Soc. **79**, 2033 (1996).

[8] M. A. Pamungkas, M. Joe, B.-H. Kim, and K.-R. Lee, J. Appl. Phys. **110**, 053513 (2011).

[9] B.-J. Lee and M. I. Baskes, Phys. Rev. B **62**, 8564 (2000).

[10] T. P. Senftle, S. Hong, M. M. Islam, S. B. Kylasa, Y. Zheng, Y. K. Shin, C. Junkermeier, R. Engel-Herbert, M. J. Janik, H. M. Aktulga, et al., npj Comput. Mater. **2**, 1 (2016).

[11] S. Watanabe, W. Li, W. Jeong, D. Lee, K. Shimizu, E. Mimanitani, Y. Ando, and S. Han, J. Phys. Energy **3**, 012003 (2020).

[12] P. Friederich, F. Häse, J. Proppe, and A. Aspuru-Guzik, Nat. Mater. **20**, 750 (2021).

[13] W. Jeong, D. Yoo, K. Lee, J. Jung, and S. Han, J. Phys. Chem. Lett. **11**, 6090 (2020).

[14] C. Hong, J. M. Choi, W. Jeong, S. Kang, S. Ju, K. Lee, J. Jung, Y. Youn, and S. Han, Phys. Rev. B **102**, 224104 (2020).

[15] S. Kang, Y. Kim, E. Jang, Y. Kang, and S. Han, ACS Appl. Mater. Interfaces **12**, 22012 (2020).

[16] J. M. Choi, K. Lee, S. Kim, M. Moon, W. Jeong, and S. Han, Comput. Mater. Sci. **211**, 111472 (2022).

[17] K. Lee, Y. Park, and S. Han, Phys. Rev. Mater. **6**, 113802 (2022).

[18] J. P. Perdew, K. Burke, and M. Ernzerhof, Phys. Rev. Lett. **77**, 3865 (1996).

[19] J. Sun, A. Ruzsinszky, and J. P. Perdew, Phys. Rev. Lett. **115**, 036402 (2015).

[20] M. Born and R. Oppenheimer, Annalen der Physik **389**, 457 (1927).

[21] P. Hohenberg and W. Kohn, Phys. Rev. **136**, B864 (1964).

[22] W. Kohn and L. J. Sham, Phys. Rev. **140**, A1133 (1965).

[23] R. G. Parr, in *Horizons of Quantum Chemistry: Proceedings of the Third International Congress of Quantum Chemistry Held at Kyoto, Japan, October 29-November 3, 1979* (Springer, 1980), pp. 5–15.

[24] P. Ziesche, S. Kurth, and J. P. Perdew, Comput. Mater. Sci. **11**, 122 (1998).

[25] J. Sun, R. C. Remsing, Y. Zhang, Z. Sun, A. Ruzsinszky, H. Peng, Z. Yang, A. Paul, U. Waghmare, X. Wu, et al., Nat. Chem. **8**, 831 (2016).

[26] J. Behler and M. Parrinello, Phys. Rev. Lett. **98**, 146401 (2007).

[27] K. Lee, D. Yoo, W. Jeong, and S. Han, Comput. Phys. Commun. **242**, 95 (2019).

[28] J. Behler, J. Chem. Phys. **134**, 074106 (2011).

[29] B. Lakshminarayanan, A. Pritzel, and C. Blundell, in *Advances in neural information processing systems 30* (2017), pp. 6405–6416.

[30] P. Gorai, V. Stevanović, and E. S. Toberer, Nat. Rev. Mater. **2**, 1 (2017).

[31] D. R. Clarke and S. R. Phillpot, Mater. Today **8**, 22 (2005).

[32] X. C. Tong, *Advanced materials for thermal management of electronic packaging*, vol. 30 (Springer Science & Business Media, 2011).

[33] X. Qian, J. Zhou, and G. Chen, Nat. Mater. **20**, 1188 (2021).

[34] F. Zhou, W. Nielson, Y. Xia, V. Ozoliņš, et al., Phys. Rev. Lett. **113**, 185501 (2014).

[35] O. Hellman, P. Steneteg, I. A. Abrikosov, and S. I. Simak, Phys. Rev. B **87**, 104111 (2013).

[36] F. Eriksson, E. Fransson, and P. Erhart, Adv. Theory Simul. **2**, 1800184 (2019).

[37] R. McKinney, P. Gorai, E. S. Toberer, and V. Stevanovic, Chem. Mater. **31**, 2048 (2019).

[38] C. Toher, C. Oses, J. J. Plata, D. Hicks, F. Rose, O. Levy, M. de Jong, M. Asta, M. Fornari, M. B. Nardelli, et al., Phys. Rev. Mater. **1**, 015401 (2017).

[39] H. Xie, J. Yan, X. Gu, and H. Bao, J. Appl. Phys. **125**, 205104 (2019).

[40] C. Verdi, F. Karsai, P. Liu, R. Jinnouchi, and G. Kresse, npj Comput. Mater. **7**, 156 (2021).

[41] P. Korotaev, I. Novoselov, A. Yanilkin, and A. Shapeev, Phys. Rev. B **100**, 144308 (2019).

[42] B. Mortazavi, E. V. Podryabinkin, I. S. Novikov, T. Rabczuk, X. Zhuang, and A. V. Shapeev, Comput. Phys. Commun. **258**, 107583 (2021).

[43] R. Li, Z. Liu, A. Rohskopf, K. Gordiz, A. Henry, E. Lee, and T. Luo, Appl. Phys. Lett. **117**, 152102 (2020).

[44] Z. Liu, X. Yang, B. Zhang, and W. Li, ACS Appl. Mater. Interfaces **13**, 53409 (2021).

[45] J. Deng and L. Stixrude, Geophys. Res. Lett. **48**, e2021GL093806 (2021).

[46] X. Qian, S. Peng, X. Li, Y. Wei, and R. Yang, Mater. Today Phys. **10**, 100140 (2019).

[47] Z. Zeng, C. Zhang, Y. Xia, Z. Fan, C. Wolverton, and Y. Chen, Phys. Rev. B **103**, 224307 (2021).

[48] A. P. Bartók, M. C. Payne, R. Kondor, and G. Csányi, Phys. Rev. Lett. **104**, 136403 (2010).

[49] A. V. Shapeev, Multiscale Modell. Simul. **14**, 1153 (2016).

[50] G. Kresse and J. Furthmüller, Comput. Mater. Sci. **6**, 15 (1996).

[51] G. Kresse and J. Furthmüller, Phys. Rev. B **54**, 11169 (1996).

[52] G. Kresse and J. Hafner, Phys. Rev. B **47**, 558 (1993).

[53] A. Belsky, M. Hellenbrandt, V. L. Karen, and P. Luksch, Acta. Crystallogr. B **58**, 364 (2002).

[54] W. Li, J. Carrete, N. A. Katcho, and N. Mingo, Comput. Phys. Commun. **185**, 1747 (2014).

[55] A. Togo, L. Chaput, and I. Tanaka, Phys. Rev. B **91**, 094306 (2015).

[56] A. Togo and I. Tanaka, Scr. Mater. **108**, 1 (2015).

[57] N. Srivastava, G. Hinton, A. Krizhevsky, I. Sutskever, and R. Salakhutdinov, J. Mach. Learn. Res. **15**, 1929 (2014).

[58] A. P. Thompson, H. M. Aktulga, R. Berger, D. S. Bolintineanu, W. M. Brown, P. S. Crozier, P. J. in 't Veld, A. Kohlmeyer, S. G. Moore, T. D. Nguyen, et al., Comput. Phys. Commun. **271**, 108171 (2022).

[59] R. Schmid-Fetzer, J. Phase Equilib. Diffus. **35**, 735 (2014).

[60] U. R. Kattner, Tecnol. Metal., Mater. Min. **13**, 3 (2016).

[61] J.-C. Zhao, *Methods for phase diagram determination* (Elsevier, 2011).

[62] S.-M. Liang and R. Schmid-Fetzer, J. Eur. Ceram. Soc. **38**, 4768 (2018).

[63] D. Frenkel and B. Smit, *Understanding molecular simulation: from algorithms to applications* (Elsevier, 2001).

[64] D. Frenkel and A. J. Ladd, J. Chem. Phys. **81**, 3188 (1984).

[65] C. Vega, E. Sanz, J. Abascal, and E. Noya, J. Phys.: Condens. Matter **20**, 153101 (2008).

[66] U. R. Pedersen, F. Hummel, G. Kresse, G. Kahl, and C. Dellago, Phys. Rev. B **88**, 094101 (2013).

[67] D. A. Kofke and E. D. Glandt, Mol. Phys. **64**, 1105 (1988).

[68] L. Vočadlo and D. Alfè, Phys. Rev. B **65**, 214105 (2002).

[69] O. Sugino and R. Car, Phys. Rev. Lett. **74**, 1823 (1995).

[70] L. Burakovsky, N. Burakovsky, and D. Preston, Phys. Rev. B **92**, 174105 (2015).

[71] L.-F. Zhu, B. Grabowski, and J. Neugebauer, Phys. Rev. B **96**, 224202 (2017).

[72] F. Dorner, Z. Sukurma, C. Dellago, and G. Kresse, Phys. Rev. Lett. **121**, 195701 (2018).

[73] L. Burakovsky, N. Burakovsky, M. Cawkwell, D. Preston, D. Errandonea, and S. Simak, Phys. Rev. B **94**, 094112 (2016).

[74] J. Wu, F. González-Cataldo, and B. Militzer, Phys. Rev. B **104**, 014103 (2021).

[75] P. Williams, Y. Mishin, and J. Hamilton, Modell. Simul. Mater. Sci. Eng. **14**, 817 (2006).

[76] Y. Mishin, Acta Mater. **52**, 1451 (2004).

[77] D. De Fontaine, in *Solid State Phys.* (Elsevier, 1994), vol. 47, pp. 33–176.

[78] T. Tanaka, *Methods of statistical physics* (Cambridge University Press, 2002).

[79] L. G. Ferreira, C. Wolverton, and A. Zunger, J. Chem. Phys. **108**, 2912 (1998).

[80] A. van de Walle and G. Ceder, J. Phase Equilib. **23**, 348 (2002).

[81] A. van de Walle and M. Asta, Modell. Simul. Mater. Sci. Eng. **10**, 521 (2002).

[82] J. Sanchez, J. Stark, and V. Moruzzi, Phys. Rev. B **44**, 5411 (1991).

[83] A. Seko, F. Oba, A. Kuwabara, and I. Tanaka, Phys. Rev. B **72**, 024107 (2005).

[84] A. H. Nguyen, C. W. Rosenbrock, C. S. Reese, and G. L. Hart, Phys. Rev. B **96**, 014107 (2017).

[85] A. Zunger, S.-H. Wei, L. Ferreira, and J. E. Bernard, Phys. Rev. Lett. **65**, 353 (1990).

[86] A. P. Bartók, J. Kermode, N. Bernstein, and G. Csányi, Phys. Rev. X **8**, 041048 (2018).

[87] H. Zong, G. Pilania, X. Ding, G. J. Ackland, and T. Lookman, npj Comput. Mater. **4**, 48 (2018).

[88] I. A. Kruglov, A. Yanilkin, A. R. Oganov, and P. Korotaev, Phys. Rev. B **100**, 174104 (2019).

[89] H. Niu, L. Bonati, P. M. Piaggi, and M. Parrinello, Nat. Commun. **11**, 2654 (2020).

[90] V. Ladygin, I. Beniya, E. Makarov, and A. Shapeev, Phys. Rev. B **104**, 104102 (2021).

[91] H. Muhli, X. Chen, A. P. Bartók, P. Hernández-León, G. Csányi, T. Ala-Nissila, and M. A. Caro, Phys. Rev. B **104**, 054106 (2021).

[92] R. Jinnouchi, J. Lahnsteiner, F. Karsai, G. Kresse, and M. Bokdam, Phys. Rev. Lett. **122**, 225701 (2019).

[93] R. Jinnouchi, F. Karsai, and G. Kresse, Phys. Rev. B **100**, 014105 (2019).

[94] L. Zhang, H. Wang, R. Car, and E. Weinan, Phys. Rev. Lett. **126**, 236001 (2021).

[95] P. Liu, C. Verdi, F. Karsai, and G. Kresse, Phys. Rev. B **105**, L060102 (2022).

[96] C. W. Rosenbrock, K. Gubaev, A. V. Shapeev, L. B. Pártay, N. Bernstein, G. Csányi, and G. L. Hart, npj Comput. Mater. **7**, 24 (2021).

[97] X.-G. Li, C. Hu, C. Chen, Z. Deng, J. Luo, and S. P. Ong, Phys. Rev. B **98**, 094104 (2018).

[98] G. Imbalzano and M. Ceriotti, Phys. Rev. Mater. **5**, 063804 (2021).

[99] W. Jeong, K. Lee, D. Yoo, D. Lee, and S. Han, J. Phys. Chem. C **122**, 22790 (2018).

[100] G. Kresse and D. Joubert, Phys. Rev. B **59**, 1758 (1999).

[101] J. Ning, J. W. Furness, and J. Sun, Chem. Mater. **34**, 2562 (2022).

[102] S. Kang, W. Jeong, C. Hong, S. Hwang, Y. Yoon, and S. Han, npj Comput. Mater. **8**, 108 (2022).

[103] M. Rang and G. Kresse, Phys. Rev. B **99**, 184103 (2019).

[104] J.-P. Harvey, A. Gheribi, and P. Chartrand, Phys. Rev. B **86**, 224202 (2012).

[105] J. K. Johnson, J. A. Zollweg, and K. E. Gubbins, Mol. Phys. **78**, 591 (1993).

[106] B. Sadigh, P. Erhart, A. Stukowski, A. Caro, E. Martinez, and L. Zepeda-Ruiz, Phys. Rev. B **85**, 184203 (2012).

[107] T. Schneider and E. Stoll, Phys. Rev. B **17**, 1302 (1978).

[108] D. J. Evans and B. L. Holian, J. Chem. Phys. **83**, 4069 (1985).

[109] P. Son and R. Bartels, J. Phys. Chem. Solids **33**, 819 (1972).

[110] K. Marklund and S. Mahmoud, Phys. Scr. **3**, 75 (1971).

[111] J. W. Furness, A. D. Kaplan, J. Ning, J. P. Perdew, and J. Sun, J. Phys. Chem. Lett. **11**, 8208 (2020).

[112] M. Sangster, G. Peckham, and D. Saunderson, J. Phys. C: Solid State Phys. **3**, 1026 (1970).

[113] D. Saunderson and G. Peckham, J. Phys. C: Solid State Phys. **4**, 2009 (1971).

[114] R. R. Reeber, K. Goessel, and K. Wang, Eur. J. Mineral. **7**, 1039 (1995).

[115] I. Suzuki, J. Phys. Earth **23**, 145 (1975).

[116] A. Rao and K. Narender, J. Thermodyn. **2014** (2014).

[117] D. K. Smith and H. Leider, J. Appl. Crystallogr. **1**, 246 (1968).

[118] M. W. Chase, *NIST-JANAF thermochemical tables (4th ed.)*, vol. 9 (American Chemical Society Washington, DC, 1998).

[119] A. F. Kohan and G. Ceder, Phys. Rev. B **54**, 805 (1996).

[120] J. Q. Broughton and X. P. Li, Phys. Rev. B **35**, 9120 (1987).

[121] R. Freitas, M. Asta, and M. de Koning, Comput. Mater. Sci. **112**, 333 (2016).

[122] A. Grossfield and D. M. Zuckerman, Annu. Rep. Comput. Chem. **5**, 23 (2009).

[123] J. Mei and J. W. Davenport, Phys. Rev. B **46**, 21 (1992).

[124] A. B. Belonoshko, S. Arapan, R. Martonak, and A. Rosengren, Phys. Rev. B **81**, 054110 (2010).

[125] R. Doman, J. Barr, R. McNally, and A. Alper, J. Am. Ceram. Soc. **46**, 313 (1963).

[126] G. Lewis and C. Catlow, J. Phys. C: Solid State Phys. **18**, 1149 (1985).

[127] W. Huang, M. Hillert, and X. Wang, Metall. Mater. Trans. A **26**, 2293 (1995).

[128] A. R. Oganov, C. J. Pickard, Q. Zhu, and R. J. Needs, Nat. Rev. Mater. **4**, 331 (2019).

[129] J. Maddox, Nature **335**, 201 (1988).

[130] C. W. Glass, A. R. Oganov, and N. Hansen, Comput. Phys. Commun. **175**, 713 (2006).

[131] U. Schroeder, M. H. Park, T. Mikolajick, and C. S. Hwang, Nat. Rev. Mater. pp. 1–17 (2022).

[132] L. C. Gallington, Y. Ghadar, L. B. Skinner, J. R. Weber, S. V. Ushakov, A. Navrotsky, A. Vazquez-Mayagoitia, J. C. Neuefeind, M. Stan, J. J. Low, et al., Materials **10**, 1290 (2017).

[133] S. S. Cheema, D. Kwon, N. Shanker, R. Dos Reis, S.-L. Hsu, J. Xiao, H. Zhang, R. Wagner, A. Datar, M. R. McCarter, et al., Nature **580**, 478 (2020).

[134] M. H. Park, Y. H. Lee, H. J. Kim, Y. J. Kim, T. Moon, K. D. Kim, J. Mueller, A. Kersch, U. Schroeder, T. Mikolajick, et al., Adv. Mater. **27**, 1811 (2015).

[135] J. Wu, Y. Zhang, L. Zhang, and S. Liu, Phy. Rev. B **103**, 024108 (2021).

[136] J. Chevalier, L. Gremillard, A. V. Virkar, and D. R. Clarke, J. Am. Ceram. Soc. **92**, 1901 (2009).

[137] A. S. Foster, A. Shluger, and R. M. Nieminen, Phys. Rev. Lett. **89**, 225901 (2002).

초 록

밀도 범함수 이론(DFT)의 발전과 계속해서 증가하는 컴퓨팅 파워 덕분에 재료의 열물성에 대한 이론적인 예측이 실현 가능해졌다. DFT 계산이 볼츠만 운송 방정식, 열역학 적분 (thermodynamic integration), 준 대정준 앙상블 (semigrand ensemble) 시뮬레이션과 같은 이론적 방법론과 결합되면, 격자 열전도도 및 상태도를 실험 정보 없이 계산할 수 있다. 그러나, 이러한 열물성 계산은 필요한 엄청난 양의 컴퓨팅 자원을 필요로하기 때문에 제한적으로만 적용되고 있다. 최근 몇 년 동안 기계학습 퍼텐셜(MLP)은 DFT의 대리 모형으로 많은 관심을 받고 있으며, 적은 비용으로 DFT에 가까운 정확도를 가지는 것이 장점이다. 많은 연구에서 MLP가 여러 시스템에 대해 제일원리 계산의 정확도로 열물성을 예측할 수 있음이 입증되었지만, 다양한 대칭성을 가지는 결정에 대한 격자열전도도 계산과 다성분계 상태도의 구축에 관한 연구가 부족한 시점이다.

따라서 본 논문은 인공신경망 퍼텐셜(NNP)을 사용한 열물성 계산을 주제로 삼았다. 먼저 다양한 대칭성과 넓은 범위의 열전도도를 갖는 결정 구조에 대해 격자 열전도도를 계산했다. NNP 훈련을 위한 일반화 가능한 데이터 세트를 구성하기 위해 무작위 변위, 포논 모드의 중첩, 또는 제일원리 분자동역학의 세 가지 방법을 테스트했다. 이들 중 가장 좋은 방법을 25개의 결정 구조에 적용해보고, DFT만을 사용한 결과와 비교하여 정확도와 계산 비용을 평가했다. 그 결과 대부분의 컴퓨팅 자원이 데이터 세트 구축에 투입되었음을 확인했고, 데이터 세트를 줄임으로써 DFT와 비교해 근소한 정확도의 손실과 함께 최대 50배의 계산 자원 절감을 실현할 수 있었다. 다음으로, NNP 분자동역학을 통해 MgO–CaO 공융계의 자유에너지를 계산해보고 액상을 포함하는 전체 상태도를 구축했다. 이를 위한 데이터 세트는 다양한 온도, 조성, 상을 학습시키기 위해서 몇 가지 조성에 대해서 NVT 또는 NPT 분자동역학 시뮬레이션을 통해 얻었다. DFT 교환-상관 에너지 근사에 대한 차이를 보기 위해 PBE와 SCAN 두 가지 범함수를 사용하여 데이터 세트를 생성했고 상태도 결과를 비교했다. 그 결과 SCAN-NNP는 실험에서 관찰된 상경계를 상당히 정확하게 재현할 수 있었고, NNP를 사용했을 때 전체 상태도 계산 비용은 순수한 DFT 계산 방식에

비해 1,000배 이상 줄일 수 있었다. 마지막으로, 상에 대한 정보 없이 화학적 조성만 주어진 경우에 대해 상태도를 구축하는 방법을 논의했다. 상압에서 3개의 고체 다형체를 나타내는 HfO_2의 상태도를 조사하기 위해, 먼저 결정구조예측 알고리즘을 사용해 후보 상을 찾았다. 이를 기반으로 훈련된 NNP로 분자동역학 시뮬레이션과 자유 에너지 계산을 통해 따른 안정상과 전이 온도를 계산했다. 본 연구의 일련의 과정이 이론에 기반한 상태도와 재료 탐색을 위한 길을 열어줄 것이라 믿는다.

주요어: 기계학습 퍼텐셜, 인공신경망 퍼텐셜, 격자 열전도도, 자유에너지 계산, 상태도

학번: 2016-20806